Physics of Fluids ARTICLE scitation.org/journal/phf

Lagrangian models of particle-laden flows with stochastic forcing: Monte Carlo, moment equations, and method of distributions analyses

Cite as: Phys. Fluids **33**, 033326 (2021); doi: 10.1063/5.0039787
Submitted: 6 December 2020 · Accepted: 22 February 2021 ·
Published Online: 26 March 2021

View Online Export Citation CrossMark

Daniel Domínguez-Vázquez,[1,a)] Gustaaf B. Jacobs,[1,b)] and Daniel M. Tartakovsky[2,c)]

AFFILIATIONS

[1]Department of Aerospace Engineering, San Diego State University, San Diego, California 92182, USA
[2]Department of Energy Resources Engineering, Stanford University, Stanford, California 94305, USA

Note: This paper is part of the special topic, In Memory of Edward E. (Ted) O'Brien.
[a)]**Electronic mail:** ddominguezvazquez@sdsu.edu
[b)]**Author to whom correspondence should be addressed:** gjacobs@sdsu.edu
[c)]**Electronic mail:** tartakovsky@stanford.edu

ABSTRACT

Deterministic Eulerian–Lagrangian models represent the interaction between particles and carrier flow through the drag force. Its analytical descriptions are only feasible in special physical situations, such as the Stokes drag for low Reynolds number. For high particle Reynolds and Mach numbers, where the Stokes solution is not valid, the drag must be corrected by empirical, computational, or hybrid (data-driven) methods. This procedure introduces uncertainty in the resulting model predictions, which can be quantified by treating the drag as a random variable and by using data to verify the validity of the correction. For a given probability density function of the drag coefficient, we carry out systematic uncertainty quantification for an isothermal one-way coupled Eulerian–Lagrangian system with stochastic forcing. The first three moment equations are analyzed with *a priori* closure using Monte Carlo computations, showing that the stochastic solution is highly non-Gaussian. For a more complete description, the method of distributions is used to derive a deterministic partial differential equation for the evolution of the joint PDF of the particle phase and drag coefficient. This equation is solved via Chebyshev spectral collocation method, and the resulting numerical solution is compared with Monte Carlo computations. Our analysis highlights the importance of a proper approximation of the Dirac delta function, which represents deterministic (known with certainty) initial conditions. The robustness and accuracy of our PDF equation were tested on one-dimensional problems in which the Eulerian phase represents either a uniform flow or a stagnation flow.

I. INTRODUCTION

Particle- and droplet-laden flows occur in many anthropogenic and natural environments. For example, the mixing of liquid fuel spray and/or solid fuel particles with turbulent gas flows determines the efficiency of many propulsion and energy systems. Environmental pollution is affected by the dispersion of aerosol particles in environmental carrier air flow.

The Eulerian–Lagrangian (EL) method provides a natural framework for the modeling of particle- and droplet-laden flows. It uses Eulerian continuum models to describe the dynamics of the ambient flow and tracks individual particles along their Lagrangian paths.[1]

A "first-principle" EL approach accounts for the surface of a finite-size particle and computes the flow over each particle. The excessive computational cost involved in these high-resolution (aka high-fidelity) simulations limits the number of particles that can be dealt with on modern computational infrastructure to hundreds.[2–4] Reduced-complexity models, such as the force coupling method[5] and filtered particle method,[6] can reduce the computational cost and increase the computationally feasible number of particles. The accuracy of these methods deteriorates near walls, which limits their range of applicability.

Process-scale problems involve a number of particles on the order of millions to billions. To handle such numbers, it is common to treat each particle as a point of zero volume, e.g., according to the Particle-Source-In-Cell (PSIC) method.[1] This method models particles' interaction with the carrier flow via singular point source terms that account for the momentum and energy exchange. The momentum and energy exchange between the point particles and the flow is determined by the (drag) force and heat transfer between the particle and the carrier phase. Analytical expressions for the force and heat transfer coefficient are available only for a few physical conditions, with limited application range.[7,8] Thus, the widely used Stokes drag law[9] is valid for steady incompressible flows at low Reynolds numbers and for spherical particles. The Maxey-Riley (MR) relation[10] accounts for unsteady effects, but it applies only to low Reynolds number and spherical particles. More general flow conditions with arbitrary Reynolds and Mach numbers require empirical corrections to the Stokes drag,[11,12] number density, slip coefficients,[13] or viscosity ratios for droplets.[14] Treatment of the energy exchange between a point particle and the ambient flow is analogous. For low Reynolds number flows over a spherical particle, the heat transfer coefficient is computed analytically; to account for high Reynolds, Mach, and/or Nusselt numbers, one has to resort to a correction factor.[7,15]

The empirical corrections depend on plethora of parameters, such as particle shape and the Reynolds and Mach numbers, that have nonlinear effects on the flow around a particle. This naturally translates into a prediction error of a point-particle model as the momentum and energy exchange are only known within certain bounds. The twin goals of alleviating this modeling inaccuracy and expanding its applicability range have inspired multiscale and data-driven modifications to the PSIC method. Thus, the multiscale method[2,3,16–19] connects accurate high-resolution simulations with the reduced point-particle method through surrogate models. The latter approximates the interphase force and heat flux with a surrogate model in a wide parameter space using high-resolution simulations in a data-driven manner. In regions of the parameter space with a large uncertainty, additional high-resolution simulations are conducted to improve the accuracy and/or validity range of the surrogate model. As more high-resolution simulations become available, the multiscale method is updated via a Bayesian procedure. This procedure yields the stochastic forcing with a computable PDF.

The presence of such a stochastic forcing in both the empirical and data-driven approaches renders solutions to the corresponding PSIC model random as well. These solutions are given in terms of a joint probability density function (PDF) of system states or their ensemble moments. Monte Carlo (MC) simulations are often used to obtain such solutions. They are easy to implement, "embarrassingly" parallel, and free of distributional assumptions; their only approximation stems from the practical need to rely on a finite number of MC realizations, N_s, to compute the sample statistics. A drawback of the MC method is its slow convergence: its sampling error decays as $1/\sqrt{N_s}$. This can make MC simulations prohibitively expensive if each realization takes a long time to compute. Various modifications of the standard MC, e.g., multilevel MC, pseudo-MC, or combinations thereof, can significantly accelerate this convergence rate, but their performance is not guaranteed especially when the goal is to compute the full PDF rather than its moments.[20,21] Other sampling-based methods, such as stochastic collocation, require nontrivial modifications[22] in order to handle hyperbolic problems with discontinuities. When the stochastic dimension and/or the noise strength become large, such methods might become slower than the standard MC even for problems with smooth solutions.[23]

Direct numerical alternatives to sampling techniques include methods based on (generalized) polynomial chaos expansions. These methods represent uncertain inputs and state variables by orthogonal polynomials of standard random variables and often exhibit spectral accuracy. Of direct relevance to high-speed compressible flows described by the Euler equations with shocks is the multi-element generalized polynomial chaos method,[24–26] which accommodates the presence of discontinuities in the stochastic space. Its computational cost might become comparable to sampling methods,[27] specifically when the stochastic dimension is large. Like their sampling-based counterparts, the direct simulation methods do not provide physical insight into the probabilistic behavior of a system, e.g., the spatiotemporal nonlocality of the statistical moments[28] and PDFs[29] of the system states.

The method of moments (MoM) alleviates some of these disadvantages by deriving deterministic equations for the statistical moments of a system state. Since the MoM is free of polynomial expansions, it does not suffer from the "curse of dimensionality," but it often requires closure approximations to be computable. It has been used to derive moment equations for high-speed flows interacting with a particle phase;[17] the closure terms were learned from the MC simulations. Practical considerations limit the MoM to the derivation and solution of equations for the first two moments—mean and (co)variance—of a system state, which limits its usefulness for highly non-Gaussian phenomena. Specifically, the MoM cannot capture rare events occuring in such problems, which are characterized by fat-tailed PDFs.

The method of distributions (MoD) overcomes this limitation by deriving a deterministic equation for either the joint PDF or the joint cumulative density function (CDF) of the system states. Having its origins in the statistical theory of turbulence,[30] the MoD has since been used as an efficient uncertainty quantification technique.[31] It retains all the advantages of the MoM, but it might require closure approximations. The MoD yields a closed-form PDF/CDF equation for nonlinear flows in the absence of a shock, e.g., those described by the inviscid Burgers equation[32] and the shallow-water equations.[33] Within the MoD framework, shocks and discontinuities can be treated either analytically, as was done for the Buckley–Leverett equation[34] and water hammer equations,[35] or by adding the PDF/CDF equation a kinetic defect-like source term that generally has to be learned from Monte Carlo runs.[36] Numerical solutions of PDF/CDF equations admit high-order spectral accuracy[32] and can be up to two orders of magnitude faster than the standard MC.[37]

We deploy the MoD to describe isothermal particle-laden flows driven by stochastic forcings. The underlying flow model relies on the Lagrangian point-particle formulation with one-way coupling between fluid flow and particle transport. The drag on a particle is modeled as a random variable with a prescribed PDF. The MoD yields a closed-form partial differential equation for the joint PDF of a particle's position and velocity. We consider two canonical flow scenarios, both in one spatial dimension: a uniform carrier flow and a stagnation carrier flow. These are important in their own right and can be used as building blocks of more general and multi-dimensional flows; for example, the stagnation flow is a central component to the dynamic description of attractors and repellers in dynamic systems.[38] Our PDF solutions are validated against high-fidelity MC simulations and compared with solutions of the moment equations.[17] The hyperbolic PDF equation is solved via the Chebyshev collocation method.[32] Discontinuities in its solution are captured using the filtering techniques.[39,40] A key result of our analysis is the derivation of analytical expressions for the position and velocity of a particle moving in deterministic uniform and stagnation flows. These expressions allow us to generate sufficiently large numbers of MC realizations. In both flow regimes, the PDF solutions are non-Gaussian and their moments can increase or decrease depending largely on the time-dependent increase or decrease in the inter-phase velocity. Moreover, the stochastic solution can develop discontinuities at inflection points of the inter-phase velocity.

In Sec. II, we formulate an Eulerian–Lagrangian stochastic model of particle-laden flows. The formulation is presented in one-dimension but applies to multiple spatial dimensions as well. Its statistical treatment is presented in Sec. III via the MoD (Sec. III A) and the MoM (Sec. III B). Our numerical strategy for solving the resulting PDF equation is described in Sec. IV. We apply our methodology to the uniform and stagnation flows, for which the analytical solutions are derived in Sec. V. In Sec. VI, we use these two canonical settings to analyze the accuracy and robustness of the MoD and MoM solutions. Section VII contains concluding remarks and future work.

II. LAGRANGIAN PROBLEM FORMULATION

Dynamics of an isothermal collisionless particle phase in a one-way coupled unidimensional Eulerian–Lagrangian system with the point-particle approximation is governed by[1,41]

$$\frac{\mathrm{d}x_\mathrm{p}}{\mathrm{d}t} = u_p, \tag{1a}$$

$$\frac{\mathrm{d}u_\mathrm{p}}{\mathrm{d}t} = \phi\frac{u-u_p}{\tau_p}. \tag{1b}$$

Here, t is the non-dimensional time, x_p is the non-dimensional particle position, and u_p is the non-dimensional particle velocity. The non-dimensional particle response time τ_p is a measure of the response of the particle to a change in the carrier velocity u. It is expressed as $\tau_p = d_p^2 Re/(18\varepsilon)$, where $d_p = d_p^*/L$ is the non-dimensional particle diameter, $Re = U_\infty L/\nu$ is the Reynolds number, L is a characteristic length, U_∞ is the reference velocity, and $\varepsilon = \rho/\rho_p$ is the relative density ratio of the two phases.

The function ϕ is used to correct the Stokes drag force for flow conditions outside of Stokes assumptions. Such models for the corrected drag coefficient ϕ are empirical and, therefore, can only be determined within an uncertainty bound.[2,3,42] For the sake of generality, we postulate[32,42] that ϕ depends on the relative velocity $u-u_p$

$$\phi = ag(u-u_p), \tag{2}$$

without specifying the functional dependence of the function $g(\cdot)$. This function can be expanded in terms of several random modes. Here, we consider the first of those random modes and take $\phi = a$. The random coefficient a with a given PDF $f_a(A)$ accounts for the uncertainty in ϕ stemming from a broad range of sources, such as uncertainty in the particle size, shape, or inexactness/empicism of the drag force, and renders the system of ordinary differential equations (1) stochastic. Its solution is given in terms of the joint PDF $f_{ax_pu_p}(A, X_p, U_p; t)$.

Our model formulation ignores inter-particle collisions. This is justified if the particle phase is dilute, specifically in one spatial dimension.[43]

III. SOLUTION STRATEGIES

A. Method of distributions

When applied to Eq. (1), the MoD yields an exact PDF equation (see Appendix A)

$$\frac{\partial f_{ax_pu_p}}{\partial t} + \frac{\partial}{\partial X_p}\left[U_p f_{ax_pu_p}\right] + \frac{\partial}{\partial U_p}\left[\frac{Ag(U-U_p)}{\tau_p}(U-U_p)f_{ax_pu_p}\right] = 0, \tag{3}$$

with A, X_p, and U_p denoting the deterministic versions of the stochastic variables a, x_p, and u_p. Equation (3) describes the evolution of the joint PDF of the particle phase and drag coefficient, $f_{ax_pu_p}(A, X_p, U_p; t)$, in the phase space Ω spanned by coordinates (X_p, U_p, A). This space can be either infinite or bounded, $\Omega = [X_p^0, X_p^1] \times [U_p^0, U_p^1] \times [A^0, A^1]$. In the latter case, (3) is subject to boundary conditions for the independent variables X_p and U_p

$$f_{ax_pu_p}(A, X_p^b, U_p; t) = f^{X_p}_{ax_pu_p}(A, U_p; t), \tag{4}$$

$$f_{ax_pu_p}(A, X_p, U_p^b; t) = f^{U_p}_{ax_pu_p}(A, X_p; t). \tag{5}$$

The boundary functions on the right hand side of these expressions are specified according to the corresponding marginal distributions; and using the characteristic velocities of (3) defined as in Eqs. (14) and (15), $X_p^b = X_p^0$ or $X_p^b = X_p^1$ for $C_X(X_p^0) > 0$ and $C_X(X_p^1) < 0$, respectively. Similarly, $U_p^b = U_p^0$ or $U_p^b = U_p^1$ for $C_U(U_p^0) > 0$ and $C_U(U_p^1) < 0$, respectively. The PDF equation (3) is also subject to the initial condition

$$f_{ax_pu_p}(A, X_p, U_p; 0) = f^0_{ax_pu_p}(A, X_p, U_p). \tag{6}$$

The function form of $f^0_{ax_pu_p}(A, X_p, U_p)$ is determined by the degree of certainty in the initial state of the system, (x_{p_0}, u_{p_0}). If it is known with certainty, i.e., deterministic, then

$$f_{ax_pu_p}(A, X_p, U_p; 0) = f_a(A)\delta(X_p - x_{p_0})\delta(U_p - u_{p_0}), \tag{7}$$

where $\delta(\cdot)$ is the Dirac delta function. We will refer to this as a deterministic initial condition (dIC). If the initial condition is not known with certainty, then we refer to it as stochastic (sIC).

Once $f_{ax_pu_p}(A, X_p, U_p; t)$ is computed from (3)–(6), the PDFs $f_{x_pu_p}(X_p, U_p; t)$, $f_{x_p}(X_p; t)$, and $f_{u_p}(U_p; t)$ are computed as its marginals via numerical integration over the respective variables (see Appendix A).

B. Method of moments

Solutions of the moment equations have been used to elucidate many salient features of stochastically forced particle-laden flows.[17] We summarize that analysis and extend it to derive third-moment equations in order to understand the degree of non-Gaussianity. The derivation starts by using the Reynolds decomposition to represent all parameters and state variables as the sums of their respective ensemble means (denoted by the overbar) and zero-mean fluctuations (denoted by the prime), e.g., $x_p = \bar{x}_p + x_p'$ with $\overline{x_p'} = 0$. Substituting these decompositions into (1) and taking the ensemble average, we obtain equations for the means

$$\frac{d\bar{x}_\mathrm{p}}{\mathrm{d}t} = \bar{u}_p, \tag{8}$$

$$\tau_p \frac{d\bar{u}_\mathrm{p}}{\mathrm{d}t} = \bar{\phi}(\bar{u} - \bar{u}_p) + \overline{\phi' u'} - \overline{\phi' u'_p}, \tag{9}$$

for the variances, $\sigma^2_{x_p} = \overline{x'^2_p}$ and $\sigma^2_{u_p} = \overline{u'^2_p}$,

$$\frac{\mathrm{d}\sigma^2_{\mathrm{x_p}}}{\mathrm{d}t} = 2\overline{x'_p u'_p}, \tag{10}$$

$$\frac{\tau_p}{2}\frac{\mathrm{d}\sigma^2_{\mathrm{u_p}}}{\mathrm{d}t} = \bar{\phi}(\overline{u'u'_p} - \sigma^2_{u_p}) + \overline{\phi' u'_p}(\bar{u} - \bar{u}_p) + \overline{\phi' u' u'_p} - \overline{\phi' u'^2_p}, \tag{11}$$

and for the third central moments, $s_{x_p} = \overline{x'^3_p}$ and $s_{u_p} = \overline{u'^3_p}$,

$$\frac{\mathrm{d}s_{\mathrm{x_p}}}{\mathrm{d}t} = 3\overline{x'^2_p u'_p}, \tag{12}$$

$$\begin{aligned} \frac{\tau_p}{3}\frac{\mathrm{d}s_{\mathrm{u_p}}}{\mathrm{d}t} &= \bar{\phi}(\overline{u'u'^2_p} - s_{u_p}) + \overline{\phi' u'^2_p}(\bar{u} - \bar{u}_p) \\ &\quad - \sigma^2_{u_p}(\overline{\phi' u'} - \overline{\phi' u'_p}) + \overline{\phi' u' u'^2_p} - \overline{\phi' u'^3_p}. \end{aligned} \tag{13}$$

As opposed to the exact PDF equation (3), these moment equations are not closed since they contain unknown mixed, higher-order moments. To render them computable, one has to introduce closure approximations such as the *a priori* closure[41,42] used to analyze the first two statistical moments or a posteriori closure as used in Eulerian formulations.[43,44]

The moment equations (9)–(13) provide insight into the deviation of the stochastic solution from its deterministic counterpart and/or general dynamics of the moments. For example, the mean dynamics, described by (8) and (9), differs from the solution of the deterministic problem (1) with the mean value of the random parameter $\bar{a}$. The difference between the deterministic equation and the averaged equation is the correlation $\overline{\phi' u'}$ and $\overline{\phi' u'_p}$. In some special cases, e.g., when the carrier flow is constant and the relative velocity is zero ($u = u_p$), the mean of the solution is the same as the deterministic solution for $\bar{a}$; the velocity deviation decreases since the right hand side of (11) contains only the damping term.

Finally, we note that the moment equations (9)–(13) are related to the PDF equation (3) as they represent the evolution of the first three moments of f_{x_p} and f_{u_p}.

C. Singularities in the stochastic solution

The characteristic velocities which can be directly inferred from (3),

$$C_X = \frac{\mathrm{d}X_\mathrm{p}}{\mathrm{d}t} = U_p, \tag{14}$$

$$C_U = \frac{\mathrm{d}U_\mathrm{p}}{\mathrm{d}t} = \frac{Ag(U - U_p)}{\tau_p}(U - U_p), \tag{15}$$

can be different which can lead to a crossover of the characteristics' paths at certain values of A. In general, hyperbolic systems when characteristics cross, a discontinuity is expected to appear in the solution. Depending on the sign of the relative velocity, $U - U_p$, we identify two settings in which the resulting discontinuities appear in the joint PDF, $f_{ax_pu_p}$ and its marginals. First, for a positive (and constant) relative velocity [Fig. 1(a)], we consider a cloud of N_a particles with uniformly spaced different drag coefficients A_i ($i = 1 \ldots N_a$) such that $A_{i+1} > A_i$. The particle with the greatest forcing, A_{N_a} (rightmost particles), moves fastest, whereas the leftmost particle with a slower response is left behind. As a result the cloud expands. For a nonlinear relative velocity, the characteristics could steepen and cross in the expansion, yielding discontinuities (not exhibited in the graph).

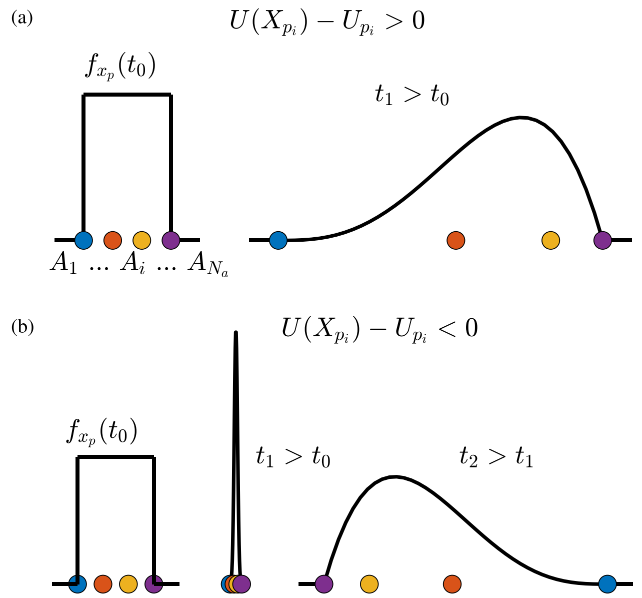

FIG. 1. Evolution of the PDF of x_p of a cloud of particles initially distributed uniformly in space and traveling at the same initial velocity (from left to right) with different drag coefficients A_i such that $A_{i+1} > A_i$. Under the influence of positive relative velocity in (a) and negative relative velocity in (b).

For a second setting, the same initial cloud is considered but for a negative (and constant) relative velocity, which causes the cloud of particles to compress. At some point, the leftmost particles overtake the rightmost particles and the cloud concentrates in a reduced region or even in a singular point. At that instant, the characteristics of the hyperbolic system (3) cross. If all of them cross in a single point, then the PDF solution becomes the Dirac delta distribution. After this singular event, the cloud expands and asymmetry can reemerge, resulting in steepening of the left side of the PDF f_{x_p} and in its discontinuity, as it did for the positive relative velocity.

Consistent with the formation of discontinuities in the marginal PDF, f_{x_p}, discontinuities also arise in the marginal PDF of the particle velocity, f_{u_p}. In Sec. V, we illustrate these phenomena by analyzing the uniform and stagnation carrier flows with stochastically forced particle dynamics.

IV. NUMERICAL IMPLEMENTATION

The discontinuities and sharp gradients that can appear in the solution of the PDF equation (3) require special numerical treatment. We use a low-dispersive/diffusive Chebyshev collocation method to approximate the derivatives with respect to X_p and U_p. Such spectral treatment was shown to be effective or even necessary to solve similar moment equations in Ref. 17. We also deploy the filtering and regularization techniques designed to capture discontinuities and regularize singularities in a spectral solution while preserving accuracy.[17,40,45,46]

A. Chebyshev collocation method and time integration

The Chebyshev collocation method, extensively described in the textbooks,[47,48] is briefly summarized below for the sake of completeness. We do so for one spatial dimension; the multi-dimensional formulation builds upon that as it is defined along lines on a tensorial grid. In the Chebyshev collocation method, a function $y(x)$ is approximated by a Chebyshev interpolant as

$$y_{N_x}(x) = \sum_{j=0}^{N_x} y(x_j) l_j(x), \quad l_j(x) = \prod_{k=0,\, k\neq j}^{N_x} \frac{x - x_k}{x_j - x_k}. \tag{16}$$

Here $j = 0, \ldots, N_x$; $l_j(x)$ is the Lagrange polynomial of degree N_x. The collocation points are chosen as the Gauss-Lobatto quadrature points

$$\xi_i = -\cos(i\pi/N_x), \quad i = 0, \ldots, N_x \tag{17}$$

such that the L_∞ norm of the interpolant is minimized on the interval $[-1, 1]$.

The derivative of the function $y(x)$ at points x_i is approximated by

$$\frac{\partial y}{\partial x}(x_i) \approx \sum_{j=0}^{N_x} y(x_j) l_j'(x_i), \tag{18}$$

with l_j' the derivative of the corresponding Lagrange polynomial. This approximated derivative is recast in the matrix-vector form

$$\mathbf{y}' = \mathbf{D}\mathbf{y}, \tag{19}$$

where the differentiation matrix $\mathbf{D}$ has components $D_{i,j} = l_j'(x_i)$.

The multi-dimensional PDF equation (3) is discretized on a tensorial grid that spans X_p, U_p, and A in the domain $\boldsymbol{\Omega}$. The spectral approximation of the distribution function $\tilde{\mathbf{f}} = \tilde{f}_{N_A N_{X_p} N_{U_p}}(A, X_p, U_p)$ on this grid is governed by the semi-discrete equation

$$\frac{\mathrm{d}\tilde{\mathbf{f}}}{\mathrm{d}t} + \mathbf{D}^{X_p}\mathbf{F}^{X_p} + \mathbf{D}^{U_p}\mathbf{F}^{U_p} = 0, \tag{20}$$

where the entries of the flux arrays are given by

$$F_{i,j,k}^{X_p} = U_{p i,j,k} \tilde{f}_{i,j,k}, \tag{21}$$

$$F_{i,j,k}^{U_p} = \frac{A_{i,j,k} g(U_{i,j,k} - U_{p i,j,k})}{\tau_p} (U_{i,j,k} - U_{p i,j,k}) \tilde{f}_{i,j,k}, \tag{22}$$

with counters i, j, k along the tensors. The matrices $\mathbf{D}^{X_p}$ and $\mathbf{D}^{U_p}$ are the scaled versions of the matrix $\mathbf{D}$ with the following entries:

$$(D^{X_p})_{m,j} = \frac{\partial \xi}{\partial X_p}(D_{m,j}), \quad (D^{U_p})_{m,k} = \frac{\partial \xi}{\partial U_p}(D)_{k,m} \tag{23}$$

with $\partial\xi/\partial X_p = 2/(X_p^{\max} - X_p^{\min})$ and $\partial\xi/\partial U_p = 2/(U_p^{\max} - U_p^{\min})$ for the one-dimensional case. The matrix-vector multiplication $\mathbf{D}^{X_p}\mathbf{F}^{X_p}$ and $\mathbf{D}^{U_p}\mathbf{F}^{U_p}$ is performed along grid lines with the counters j and k, respectively, in (21) and (22). The carrier flow velocity $\mathbf{U}$ is specified at the particle locations. The semi-discrete system is integrated in time with the total variation diminishing (TVD) Runge-Kutta scheme.[49]

To obtain the marginals, f_{x_p} and f_{u_p} are obtained via the numerical integration of $f_{a x_p u_p}$ along A and either U_p or X_p, respectively. This is done via Clenshaw-Curtis quadrature in U_p and X_p and via the trapezoidal rule in A. Because the distribution equation does not have terms with derivatives respect to A, the spectral approximation is not necessary in this direction.

B. Regularization of Dirac delta function

The numerical solution of the PDF equation (3) with the deterministic initial state (7) requires an approximation of the Dirac delta function $\delta(\cdot)$. We rely on the kernel that regularizes $\delta(\cdot)$ with a class of high-order, compactly supported polynomials,[45]

$$\delta_\varepsilon^{m,k}(x) = \begin{cases} \varepsilon^{-1} P^{m,k}(x/\varepsilon), & x \in [-\varepsilon, \varepsilon] \\ 0, & \text{otherwise}, \end{cases} \tag{24}$$

where $\varepsilon > 0$ is the support width or scaling parameter. On the compactly supported interval, the regularized delta function integrates to unity (i.e., the zeroth moment is one). The polynomial $P^{m,k}$ is designed to have the first up to the m^{th} moment vanished and to have k continuous derivatives at the endpoints of the compact support. For it to be possible for the moments to vanish the regularized delta is permitted to have negative values on its supported interval. The vanishing moments ensure that the regularized Dirac delta kernel (a so-called delta sequence) converges to the exact Dirac delta function at a rate of $\mathcal{O}(\varepsilon^{m+1})$. This moment property is necessary for the construction of high-order approximations of singular Dirac delta source terms in spectral approximations of PDEs as was shown in Ref. 45. To preserve high-order spatial accuracy, it was further shown that the optimal value for the compact support must be $\varepsilon = N_x^{-k/(m+k+2)}$. The compact kernel $\delta_\varepsilon^{m,k}(x)$ in (24) has a maximum at its center. To achieve high-order accuracy, one has to relax positivity of the kernel, leading to the undershoots in Fig. 2.

For the approximation of the initial Dirac delta distribution function in (7), the vanishing moments of the regularized delta function yield an accurate representation of the zero moments of the deterministic initial state. Thus, in that case the regularized Dirac delta provides both spatial accuracy and the correct statistical properties of the distribution function at the initial time.

A naive alternative is to approximate $\delta(x)$ via a Gaussian PDF

$$\delta(x) \approx \frac{1}{\sqrt{2\pi}\sigma_x} \exp\left[-\frac{x^2}{2\sigma_x^2}\right], \tag{25}$$

with small variance σ_x^2. The Gaussian PDF, however, has no vanishing moments and can thus not yield high-order approximations to the Dirac delta. If the initial state is random, than the Gaussian distribution does correctly represent uncertainty in the initial state of the system.

C. Filtering for capturing discontinuities

Since (3) admits singularities, we have to regularize these singularities in numerical approximations to avoid numerical instabilities. To this end, we once again resort to the regularized Dirac delta kernel

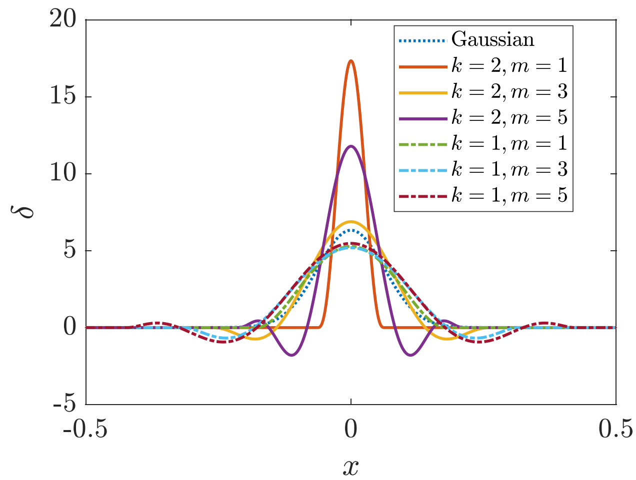

FIG. 2. Regularization of the Dirac delta function, $\delta_\varepsilon^{m,k}$, in comparison with a Gaussian PDF.

(24). This time the kernel serves as a convolution filter kernel as discussed in Ref. 40 to smoothen a function $y(x)$ as follows:

$$\tilde{y}(x) = \int_{x-\varepsilon}^{x+\varepsilon} y(\tau)\delta_\varepsilon^{m,k}(x-\tau)\mathrm{d}\tau. \tag{26}$$

Using a quadrature rule for approximation of the convolution integral, the interpolant y_{N_x} is filtered as

$$\tilde{y}_{N_x}(x) = \int_{x-\varepsilon}^{x+\varepsilon} \delta_\varepsilon^{m,k}(x-\tau)\sum_{i=0}^{N_x} y(x_i)l_i(\tau)\mathrm{d}\tau = \sum_{i=0}^{N_x} y(x_i)S_i(x). \tag{27}$$

The discrete filter S_i is defined as

$$S_i(x) = \int_{x-\varepsilon}^{x+\varepsilon} l_i(\tau)\delta_\varepsilon^{m,k}(x-\tau)\mathrm{d}\tau. \tag{28}$$

In vector notation, (27) and (28) take the form

$$\tilde{\mathbf{y}} = S\mathbf{y}. \tag{29}$$

The extension to tensorial form is straightforward. This convolution filter was shown in Ref. 40 to smoothen shock discontinuities while providing high-order accurate resolution away from shocks. In some cases, a weak exponential filter[32] is needed to remove high-frequency numerical noise that appears in regions near the boundaries.

D. Monte Carlo simulations

The PDF and the moments of the PDF can be computed with a MC approach. In MC, realizations of x_p and u_p are computed by solving (1) with random coefficients a drawn from a given PDF $f_a(A)$. Here, we use analytical solutions that will be discussed in Sec. V and that allow for a computationally efficient determination of a significant number of MC realizations, N_s. In all the tests considered, we found $N_s = 10^5$ realizations to be sufficiently accurate yielding a normalized error of the third moment less than 0.1%. The kernel density estimation, implemented in the Matlab 2019b subroutine kdensity, determines the PDFs $f_{x_p}(X_p;t)$, $f_{u_p}(U_p;t)$, and $f_{x_pu_p}(X_p,U_p;t)$. The unknown correlation terms in the moment equations (8)–(13) are closed using MC realizations. The resulting *a priori* closed moment equations are integrated in time via the fourth-order Runge-Kutta (RK4) scheme.

V. TWO CANONICAL PARTICLE-LADEN FLOWS

We consider two one-way coupled particle-laden flows—a uniform flow and an inviscid stagnation flow—for which the carrier phase velocity is described by analytical expressions. These are both important in their own right and serve as building blocks for more complex flows. Both flows admit analytical solutions for the corresponding particle-laden flow with constant deterministic forcing, $\phi = $ constant. While this particle solution for the uniform carrier flow is well known, we are not aware of an analytical solution to the particle-laden stagnation flow. Analytical solutions are derived for both flows in Secs. V A and V B.

A. Uniform flow

By its definition, a uniform carrier flow is characterized by a constant velocity field u. To derive the analytical solution, we cast the particle transport equations (1) with the constant u and the initial conditions $x_p(0) = x_{p_0}$ and $u_p(0) = u_{p_0}$ into the following linear system of ODEs:

$$\frac{\mathrm{d}}{\mathrm{d}t}\begin{bmatrix} x_p \\ u_p \end{bmatrix} = \begin{bmatrix} 0 & 1 \\ 0 & -b \end{bmatrix}\begin{bmatrix} x_p \\ u_p \end{bmatrix} + \begin{bmatrix} 0 \\ bu \end{bmatrix}, \quad b \equiv \frac{a}{\tau_p}. \tag{30}$$

The analytical solution of this system is

$$x_p(t) = x_{p_0} + ut + \frac{1}{b}(u - u_{p_0})(e^{-bt} - 1), \tag{31}$$

$$u_p(t) = u + (u_{p_0} - u)e^{-bt}. \tag{32}$$

Details of the derivation are provided in Appendix B.

The solution is plotted in Fig. 3 and shows that the response of the particle initially at rest to a fluid velocity is slower with increasing b, i.e., with increasing effective inertia. Hence, for a given τ_p, higher values of the correction parameter a decrease the particle's time response. At long times on the order of $\mathcal{O}(1/b)$, the particle velocity becomes equal to the carrier flow velocity u. When the relative velocity between the particle and the carrier phase (also called interphase velocity) becomes zero, the particle position increases linearly at its constant advection rate u.

B. Stagnation flow

The stagnation carrier velocity field, $\mathbf{u} = (u, v)^\top$, is given by the Hiemenz analytical solution for an inviscid, irrotational flow[50] in the domain $x \in [-\infty, 0]$ as follows:

$$u = -kx, \quad v = ky,$$

where y is the coordinate perpendicular to the flow direction, and k is a constant. (The viscous boundary layer solution near a wall at $x = 0$ is available as well.[51] It predicts the boundary layer thickness of $\delta = \sqrt{\nu/k}$, too thin to affect the particle dynamics.)

Along the centerline $y = 0$, the flow is one-dimensional with a stagnation point at $x = 0$ and velocity

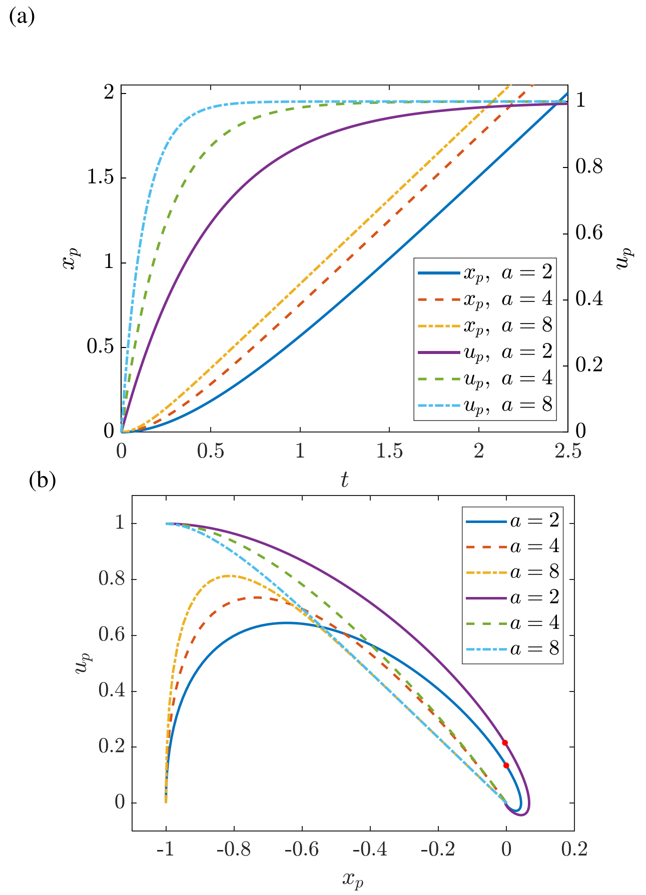

FIG. 3. Time dependence (a) and phase space (b) of the particle dynamics in the constant uniform carrier flow.

$$u = -kx. \tag{33}$$

With the carrier velocity at the particle location x_p is $u = -kx_p$ (1) can be cast into a linear dynamic system,

$$\frac{\mathrm{d}}{\mathrm{d}t}\begin{bmatrix} x_p \\ u_p \end{bmatrix} = \begin{bmatrix} 0 & 1 \\ -kb & -b \end{bmatrix}\begin{bmatrix} x_p \\ u_p \end{bmatrix}. \tag{34}$$

The analytical solution to this system is derived in Appendix B and is characterized by the eigenvalues of the 2×2 matrix in (34)

$$\lambda_1 = \frac{-b - \sqrt{b(b-4k)}}{2}, \quad \lambda_2 = \frac{-b + \sqrt{b(b-4k)}}{2}. \tag{35}$$

Their real and imaginary parts are plotted in Fig. 4, for $b \in [0, 8]$ and $k = 1$. For $0 < b < 4k$, the eigenvalues are imaginary with negative real part. In that case, the solution of the system (34), i.e., the particle phase solution, is well-known to tend toward an inward spiral in the phase plane as plotted in Fig. 5(c). Before it reaches the spiral singularity, however, the particle will have crossed the $x = 0$ line where the wall is located. This is, of course, not possible and the particle trace has to terminate at $x = 0$. Alternatively, we can interpret the solution as a physical solution of a particle trajectory in an opposed jet carrier flow.

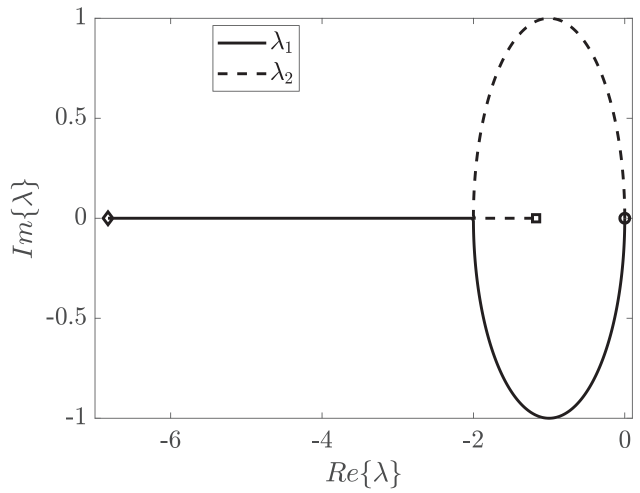

FIG. 4. Imaginary and real part of the eigenvalues λ_1 and λ_2 in (35) for $b \in [0, 8]$. The circle corresponds to $b = 0$, and the diamond and square correspond to $b = 8$ for λ_1 and λ_2, respectively.

For $b > 4k$, both eigenvalues are real and negative, in which case the particle moves toward an inward node in the phase space $x_p - v_p$. A bifurcation in particle dynamics from a spiral to a node occurs at $b = 4k$. Figure 5(c) shows the particle phase when the stagnation point is an inward node and an inward spiral for two different initial conditions.

The analytical solutions for the particle's position and velocity, $x_p(t)$ and $u_p(t)$, vs time are plotted in Figs. 5(a) and 5(b). The particle reaches the stagnation point for any forcing $b = a/\tau_p$. The collision of the particle with the wall for the stangation flow case is indicated by the red dot in the graphs 5(a), 5(b), and 5(c).

C. Impact of stochastic forcing

The effect of a stochastic forcing on the particle-laden uniform and stagnation flows is studied for the cases and parameters collated in Table I. For both flow regimes, we consider particles initialized at rest. For the stagnation flow, we also consider the particles initialized according to the carrier flow velocity.

For each of these cases, we consider three PDFs, $f_a(A)$, for the random variable a in the drag correction factor defined in (2) including a uniform, normal, and beta distribution, all with the same mean μ_a and standard deviation σ_a (Fig. 6). For the stagnation flow, $f_a(A)$ is selected to have a non-zero probability in the interval $0 < a/\tau_p < 4k$ to ensure that all particles reach the wall at a finite time (according to the deterministic solution). Also investigated is the effect of deterministic vs stochastic initial conditions.

VI. SIMULATION RESULTS AND DISCUSSION

A. Uniform flow: Monte Carlo results

The PDFs $f_{x_p}(X_p; t)$ and $f_{u_p}(U_p; t)$ obtained via MC solution of (1) for the uniform flow with the uniform forcing distribution $f_a(A)$ and deterministic initial conditions are depicted in Fig. 7. Starting from the deterministic Dirac delta initial distribution, both $f_{x_p}(X_p; t)$ and $f_{u_p}(U_p; t)$ first widen over time, while showing a skewness, i.e., a

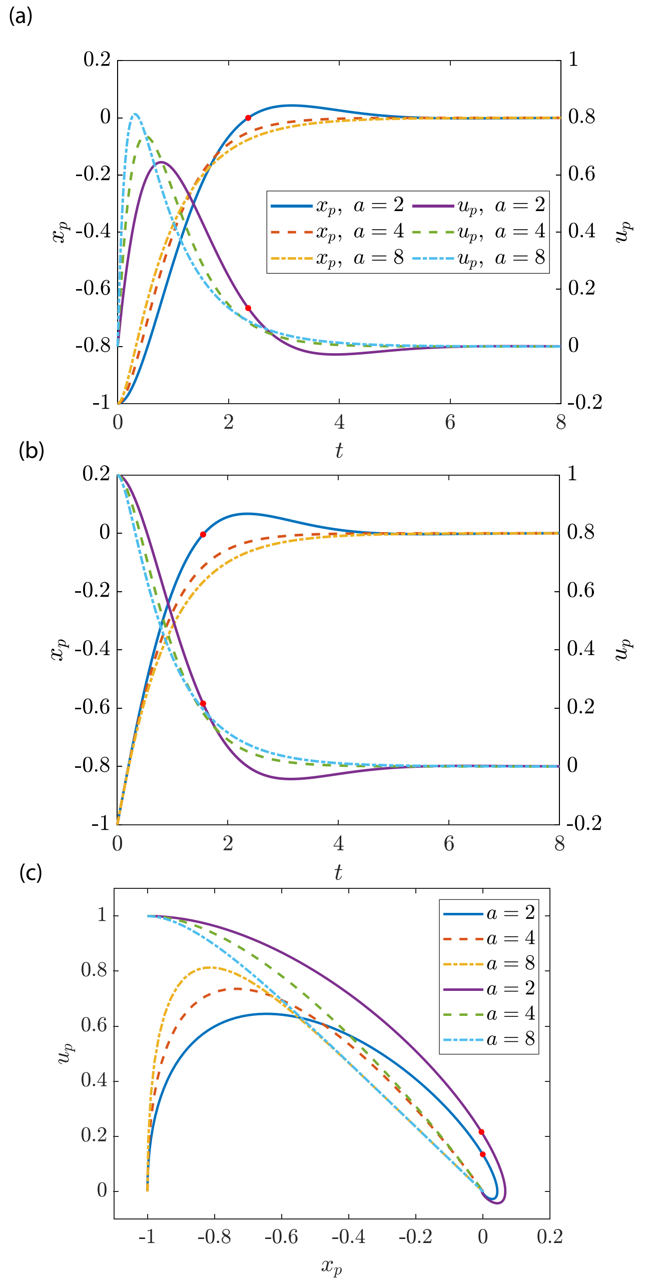

FIG. 5. Solutions for particles released at rest (a) and at flow condition (b) in a stagnation flow with $k=1$ for different values of parameter b. The phase space plot in (c).

bias, toward the upper range of the X_p and U_p values, where more particles accumulate. This bias reflects the particles' asymptotic behavior in the limit of an infinite response time, $\tau_p \to \infty$ in which case all the particles congregate on a step function in time. After the initial widening, the velocity distribution narrows with time as the particles' velocity settles to the uniform carrier flow velocity. The temporal evolution of the PDFs has a characteristic time scale on the order $\mathcal{O}(\tau_p/\bar{a})$. At later times, the velocity distribution returns to the Dirac delta and the corresponding position distribution is advected at constant velocity u without changes in time.

The means $\bar{x}_p(t)$ and $\bar{u}_p(t)$, plotted with their corresponding two standard deviation bandwidths in Fig. 8, tell a similar story. The mean particle velocity $\bar{u}_p(t)$ increases from its zero initial state and settles to the constant carrier velocity at $t \to \infty$. Associated with the acceleration and settling is an initial increase in the velocity bandwidth that then returns to zero at later times. Consistent with the velocity bandwidth, the position bandwidth grows initially and then remains constant when the particles settle.

Per definition, and as confirmed by Fig. 8, the mean of the solution must be contained in the interval of deterministic limit trajectories. Moreover, because $x_p(a)$ and $u_p(a)$ are monotonically increasing with a, it follows that

$$\bar{x}_p \in \left[\min_a\{x_p(a_{\min}), x_p(a_{\max})\}, \max_a\{x_p(a_{\min}), x_p(a_{\max})\}\right],$$
$$\bar{u}_p \in \left[\min_a\{u_p(a_{\min}), u_p(a_{\max})\}, \max_a\{u_p(a_{\min}), u_p(a_{\max})\}\right],$$

where $a_{\min} > 0$ and $a_{\max}$ denote a minimum and maximum value of a. This suggests that $\bar{x}_p \approx x_p(\bar{a})$ and $\bar{u}_p \approx u_p(\bar{a})$, i.e., the mean solution is equal to the deterministic solution at the mean stochastic forcing.

The moment equations provide further insight. Because of the correlation terms $\overline{\phi' u'}$ and $\overline{\phi' u_p'}$, the governing equations for the

TABLE I. Flow regimes and parameter values considered in the simulations.

Test case	x_{p_0}	u_{p_0}	u	τ_p
Uniform flow, particle launched at rest (UF)	0	0	1	0.25
Stagnation flow, particle launched at rest (SFR)	−1	0	$-x_p$	1
Stagnation flow, particle launched at flow conditions (SFF)	−1	1	$-x_p$	1

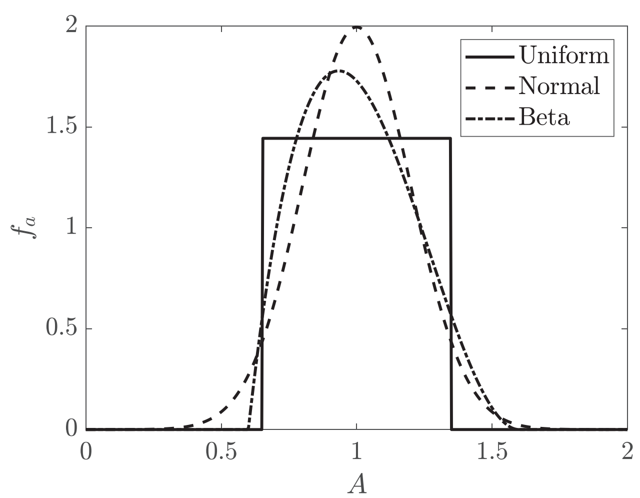

FIG. 6. Uniform, normal, and beta ($\mathcal{U}$, $\mathcal{N}$, $\mathcal{B}$) PDFs selected for the random parameter a. All three PDFs have the same mean $\mu_a = 1$ and standard deviation $\sigma_a = 0.2$, i.e., $a \sim \mathcal{U}[1-\sqrt{12}/2, 1+\sqrt{12}/2]$, $a \sim \mathcal{N}[1, 0.2]$, and $a \sim \mathcal{B}[2,3] + 0.6$.

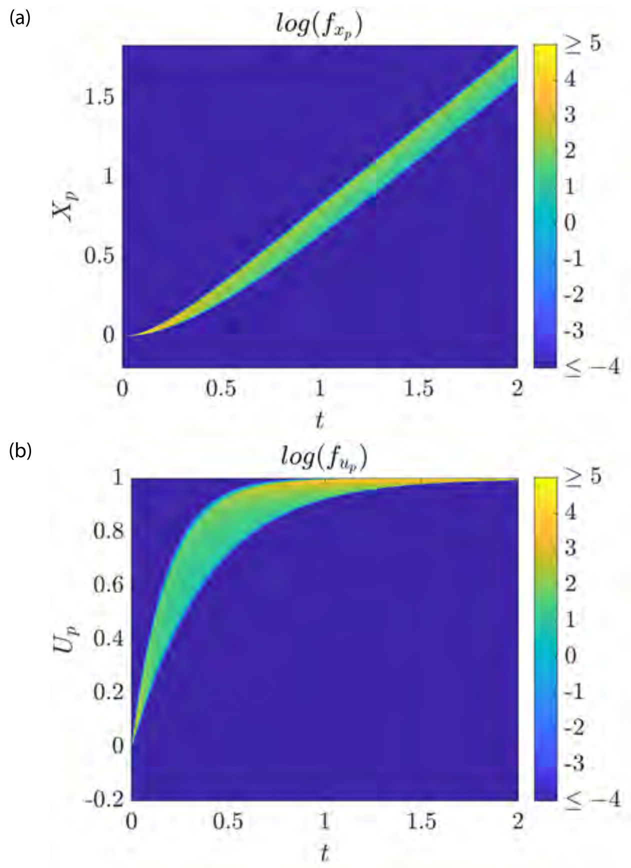

FIG. 7. PDF of particle position (a) and velocity (b) for the UF test case carried out with MC with a uniform forcing distribution.

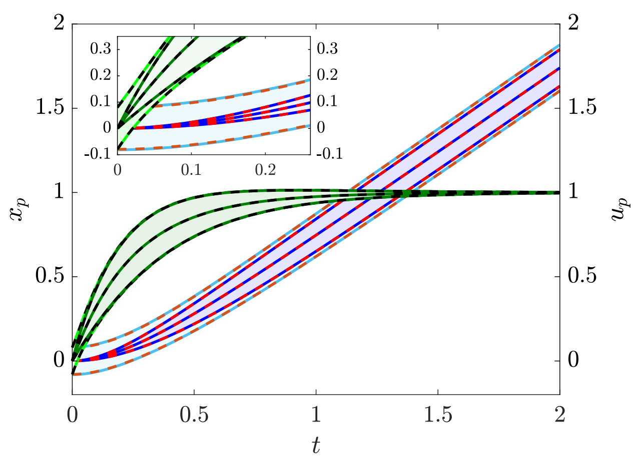

FIG. 8. Two standard deviation interval along the mean for the test case UF with a uniform forcing distribution. In dashed green, the particle velocity computed with MoD and in black with MC. In dashed red, the particle position computed with MoD and in blue with MC. Dark colors indicate dIC, whereas light ones indicate sIC.

mean position and velocity in (8) and (9), respectively, are different from the deterministic equations (1) with $a = \bar{a}$. But the term $\overline{\phi' u'}$ is zero for the uniform flow case because $u' = 0$. Moreover, the correlation term $\overline{\phi' u'_p}$ in (9) is negligible, but not zero. Thus, to a first approximation, $\bar{x}_p \approx x_p(\bar{a})$ and $\bar{u}_p \approx u_p(\bar{a})$. For a random solution with a uniform stochastic forcing distribution, the root mean square difference over the time interval is 0.0073 for the position and 0.0062 for the velocity.

With a zero carrier phase velocity perturbation, $u' = 0$, many of the correlation terms in the second central moment or variance of the velocity are also zero or negligible. Significant terms that remain are a damping term $-\bar{\phi}\sigma^2_{u_p}$ and the source term, $\overline{\phi' u'_p}(\bar{u} - \bar{u}_p)$. The latter is positive because the relative velocity is positive, $(\bar{u} - \bar{u}_p) > 0$, and because $\phi' = a'$ and u'_p have the same sign since the particle velocity u_p is monotonically increasing with respect to the forcing $\phi = a$. The positive source term is maximum initially and decreases as the particle velocity settles to the flow conditions. The damping term reduces the velocity variance to zero in the limit $t \to \infty$. Correspondingly, the PDF f_{u_p} tends to the Dirac delta distribution [Fig. 7(b)]. The combination of the temporal damping and forcing by the positive source leads to a maximum variance at times that are on the order of $\mathcal{O}(\tau_p/\bar{a})$. The particle position variance depicted in Fig. 9(a) shows an initial increase consistent with the increasing velocity variance and an increased spreading of random particle trajectories. When the particles settle to the constant carrier flow condition, all trajectories are advected at constant velocity. After that time, the particle variance no longer changes.

In Fig. 9(a), the variance of the particle velocity and position are plotted vs time for three different forcing distributions f_a (uniform, normal, and beta). The temporal trends for the different stochastic forcing are very similar because the mean forcing and its variance are chosen to be the same for the three forcing distributions. The damping term in the velocity variance equation, which depends on the mean forcing and velocity variance only, is therefore not affected by the shape of the forcing distribution. The source correlation term, however, is directly dependent on the forcing fluctuations, ϕ', which leads to differences in the velocity and position variances for different shapes of the forcing distribution of up to 15%.

The third central particle position and velocity moments evolve in a similar way as the variances [Fig. 9(b)]. The third velocity moment, s_{u_p}, experiences a negative growth followed by an asymptotic decay to zero (or the Dirac delta in the PDF sense as observed above). The third position moment, s_{x_p}, first decreases and then asymptotically evolves to a constant value. Both the minimum in s_{u_p} and the plateau in s_{x_p} occur at slightly later times as compared to the minimum in σ_{u_p} and σ_{x_p}. The difference in the factors $2\phi/\tau_p$ and $3\phi/\tau_p$ in Equations (11) and (13) is assumed to be at least partially responsible for causing this shift in the maximum. The similarity in variance and skewness trends would suggest that the third moment dynamics might also be primarily affected by a positive sourcing and a damping. To verify this, the correlation terms in (13) are plotted vs time in Fig. 10. Clearly, the damping term $-\bar{\phi}s_{u_p}$ has a major influence on the long term response. However, there is no single dominant source term. While the term $\overline{\phi' u'^2_p}(\bar{u} - \bar{u}_p)$ plays a similar role as the positive source term in the variance equation, the other correlation terms are not negligible and contribute also. Surprisingly perhaps is that the term with fourth order correlations, $-\overline{\phi' u'^3_p}$, is dominant, an indication that the tail behavior of the solution PDF and tail behavior of the forcing function has a

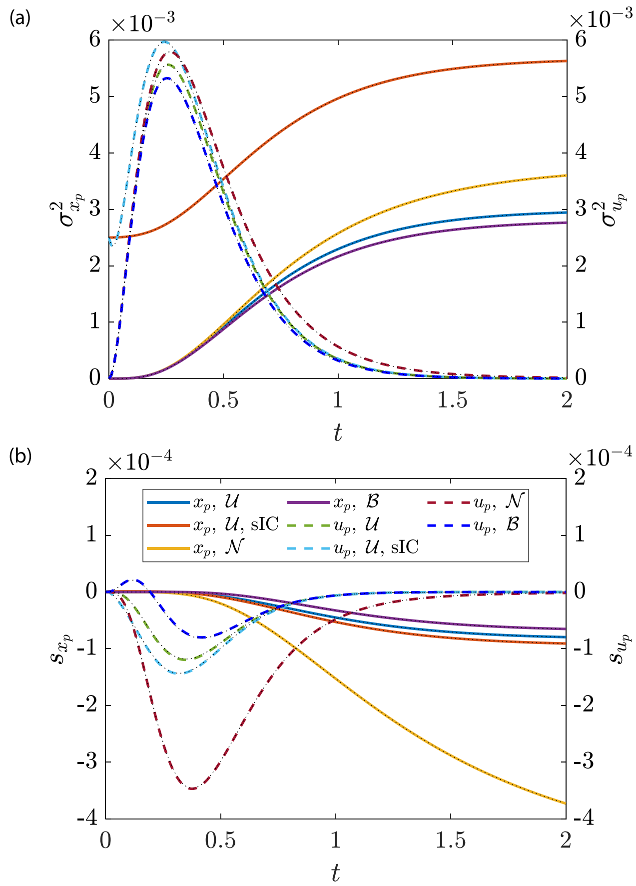

FIG. 9. Computations for the UF case with MC in color lines and with the MoM in black dots of the (a) second and (b) third central moments for the particle position and velocity and the three PDFs considered for *a* (see Fig. 6) and dIC. It is included the case of sIC for the uniform distribution. The legend in (b) is valid for (a) as well.

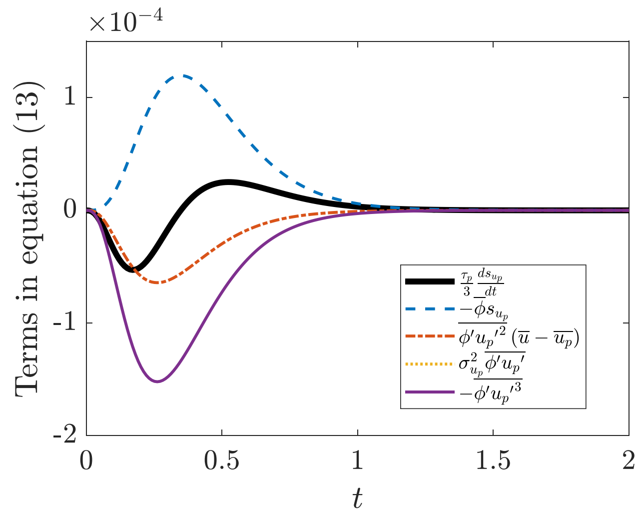

FIG. 10. Terms in Eq. (13) vs time *t* for the UF case with dIC.

considerable impact on the higher central moment solution of the solution. This is confirmed by the deviation in the third central moment evolution of up to 200% for different forcing distributions. We plan to report further on the tail behavior of the PDF in the near future.

The solution with stochastic initial condition (sIC) is plotted in Figs. 8 and 9. It shows that while the trends in the position and velocity mean and variance are similar to those determined with a deterministic initial condition (dIC), the sIC solution is offset as compared to the dIC solution. The offset is according to the initial position deviation of $\sigma_x = 0.05$. Time integration of (10) from time zero to a time t confirms that exactly this term $\sigma_x(t = 0)$ appears at the initial time, $t = 0$. The offset in Fig. 9 does not change significantly over the time interval $[0, t]$, which implies that the term $\overline{x_p' u_p'}$ in (10) is small. MC simulations confirm this and show that the term has a maximum value of 0.002 over the time interval. Because of the damping term, the velocity variance and third central moment goes to zero in the asymptotic time limit for both deterministic and stochastic initial conditions.

B. Uniform flow: Method of distributions

The solution of the governing equation for the PDF in (3) is grid-resolved for the uniform flow case using a spectral grid with $N_{X_p} \times N_{U_p} = 300 \times 300$ collocation points and a uniform grid in A direction with $N_A = 200$. The CFL condition is set to 0.8. The Dirac delta distribution function for dIC is regularized according to $\delta_\varepsilon^{k,m}$ in (24) with an optimal scaling $\varepsilon = 0.05$, and $m = 5$ zero vanishing moments and smoothness $k = 2$.

Figure 11 shows snapshots of $f_{x_p u_p}$ (contours), f_{x_p} (left and bottom axes), and f_{u_p} (right and top axes) at three consecutive times. For reference, the mean of the particle phase solution (black line) is superposed in the contour plot. At time $t = 0$, the marginals are initialized according to the regularized Dirac delta as shown in Fig. 11(a). At a later time, $t = 0.54$, the joint PDF $f_{x_p u_p}$ has traveled along the mean in the $X_p - U_p$ coordinate system and has widened and deformed [contours in Fig. 11(b)]. The marginal f_{x_p} and f_{u_p} show that the particles have a bias toward the larger values of the position and the velocity. That is consistent with the observations in the moments discussed previously; because the particles with smaller response time, τ_p/A, travel a distance greater than the slower responding particles, they cluster at large X_p. Those fast particles furthermore reach their terminal settling velocity faster and thus there is a similar clustering in f_{u_p}. The convexity of the PDFs is an indication that the clustering is more pronounced toward larger values. The schematic in Fig. 12 underscores this and shows how the characteristic paths with non-constant advection velocity for different A_i leads to a convex probability density.

At time $t = 1.6$, the velocity PDF has evolved toward a Dirac delta function represented by a narrowly supported distribution centered at $U_p = 1$. The numerical solution successfully captures this PDF behavior despite showing some minor fluctuations caused by Gibbs oscillations. The accuracy of the MoD solution at this time relies largely on the number of vanishing moments m of the regularization of the Dirac delta function at $t = 0$. Because the number of vanishing moments is specified to be greater than five, the first up to the fifth moment is accurately preserved even at times when the distribution function

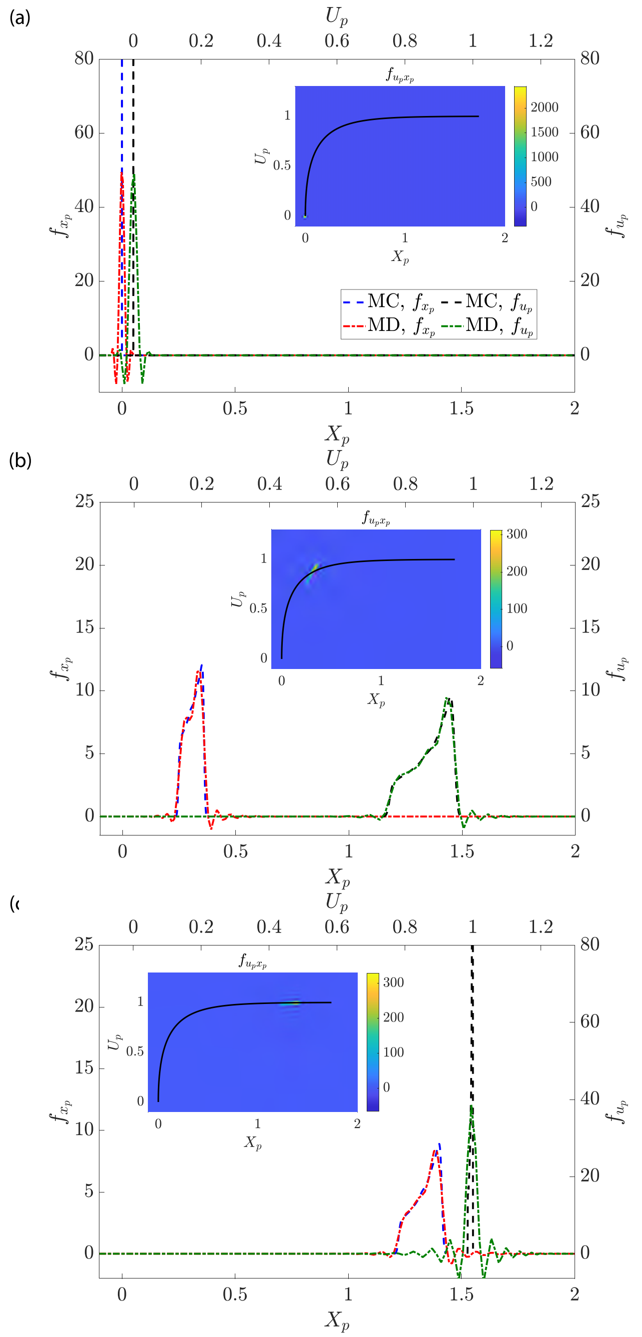

FIG. 11. Marginals f_{x_p} and f_{u_p} at $t = [0, 0.54, 1.6]$ in (*a*), (*b*), and (*c*) respectively, for the UF test case with dIC and the uniform distribution for f_a. Contour plots of the joint PDF $f_{x_p u_p}$ superposed with the mean of the particle phase solution.

tends to the singular Dirac delta distribution. This accuracy preservation is confirmed by the results in Fig. 8 that compares the time evolution of the mean and variance determined with the MoD and MC approach and that shows no discernible difference between the solutions of the two approaches.

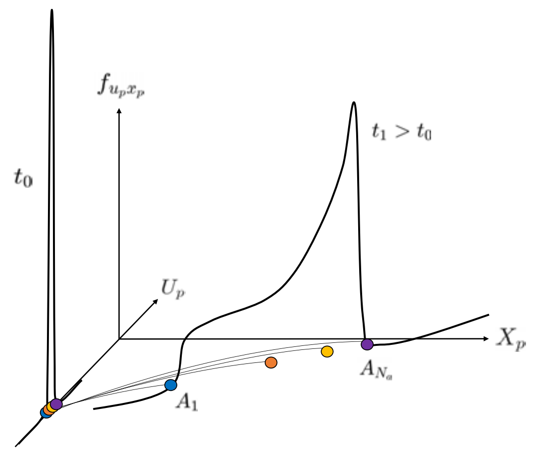

FIG. 12. Schematic evolution in time of the particle phase PDF $f_{x_p u_p}$ for the UF test case.

A few remarks on the accuracy of the numerical solution of Eq. (3):

Remark 1: Consistent with the findings in Ref. 17, the use of high order methods is necessary to compute an accurate solution of the joint PDF $f_{a x_p u_p}$ such that the marginals determined according to (A15)–(A17) are in good comparison with MC results. To underscore the importance of numerical discretization, we compare the Chebyshev spectral discretization with a first and a second order upwind finite difference (FD) schemes. Figure 13(a) shows that the FD schemes are overly dissipative as compared to the spectral method if the same number of grid points are used. The root mean square error (RMSE) between resolved MC results and the spectral solution is 0.064, whereas the RMSE for the first and second order FD method is significantly larger at 0.280 and 0.180, respectively. To mitigate the dissipation and inaccuracy, FD requires an excessive resolution for the computation of the PDF after marginalization.

Remark 2: The spectral solution shows dispersion errors in the form of high-frequency oscillations in the distribution function. These are induced by the high-order approximation of the steep gradients in the PDF that in turn are a result of the steep gradient in the uniform forcing distribution f_a. These dispersion errors, however, average out and turn out to have no significant effect on the numerical accuracy of the first three moments [see Fig. 13(b) for the third central moment]. The second order FD scheme also exhibits dispersion errors, but the FD's oscillations do not average out and the moments are not accurately captured using this discretization.

Remark 3: For deterministic initial conditions, the regularization of the Dirac delta is necessary to accurately compute the moments of the evolving distribution function. Particularly, the vanishing moment condition ensures that the evolution of the third moment [Fig. 13(b)] is not affected by the numerical approximation as compared to Dirac delta regularization with only two vanishing moment $m = 2$ in (24), or a Gaussian distribution function.

C. Stagnation flow

In the particle-laden stagnation flow, the relative (interphase) velocity is not only affected by the evolution of the particle phase as is

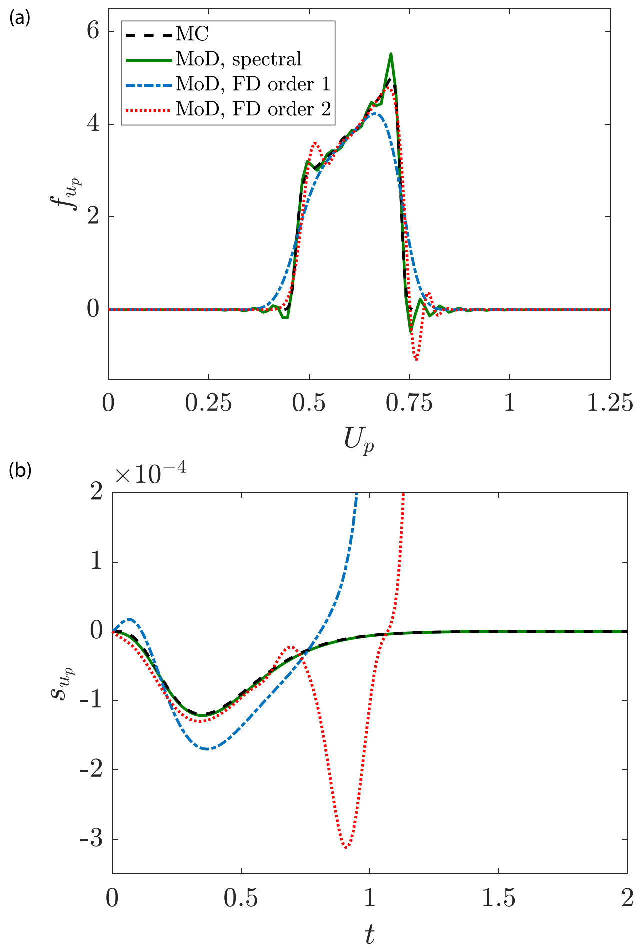

FIG. 13. Comparison between the spectral discretization and finite difference upwind discretization with first and second order for (a) f_{u_p} at $t = 0.24$ and (b) s_{u_p}. Both figures are for the UF test case with dIC with a uniform forcing distribution.

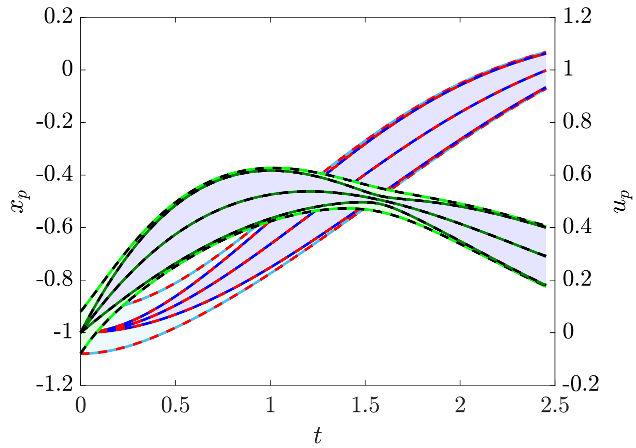

FIG. 14. Two standard deviation interval along the mean for the test case SFR with a uniform forcing distribution. In dashed green, the particle velocity computed with the MoD and in black with MC. In dashed red, the particle position computed with MoD and in blue with MC. Dark colors indicate dIC, whereas light ones indicate sIC.

the case in the uniform flow but also by the evolution of the carrier phase velocity along the particle's path. The temporal development of the random particle position and velocity, therefore, displays a considerably more complex behavior as compared to the uniform flow. Because of the spatial dependence of the carrier flow, the particle solution is furthermore non-trivially dependent on its initial condition. We consider two initial conditions described in Sec. I, one with the particles starting at rest (Case SFR) and another with the initial particle velocity specified at the carrier flow's velocity conditions (Case SFF). We discuss the MC and MoD solutions for each case below.

1. SFR case: Monte Carlo results

The mean trends with two standard deviation bandwidth determined with the MC approach for a uniform forcing distribution are plotted in Fig. 14. To discuss the SFR case, three stages of development are identified. In the first stage ($t < 0.6$) each particle identified with a counter i accelerates in positive x-direction at a rate $a_i(-kx_{p_i} - ku_{p_i})/\tau_p$. Similar to the uniform flow case, the velocity and position variance both increase in this stage with varying acceleration of the stochastically forced particles. The second central moment plotted vs time in Fig. 15(a) confirms the growth of the particle variance in this stage.

In a second stage ($0.6 < t < 1.6$), the particle with the smallest response time τ_p/a_{max}—the fastest responding particle with acceleration rate $a_{max}(-kx_{p_{max}} - ku_{p_{max}})/\tau_p$—has accelerated to the carrier velocity ($t = 0.6$). After that, the flow velocity continues to decrease (stagnates) along this particle's path. Because of the particle's inertial response, the particle's velocity, however, does not decrease equally fast along the particle's path. Effectively, the relative velocity of this particle therefor becomes negative. In other words, the particle starts to decelerate. As more particles with larger response time reach the carrier flow conditions, more particles start to decelerate until all particles have a negative relative velocity. During this second stage, the velocity variance of the particle phase decreases to a minimum at $t \sim 1.6$ [Fig. 15(a)].

In a third stage $t > 1.6$, when the relative particle velocity is smaller than zero ($u_p > u(x_p)$) for all the particles, the cloud decelerates to a decreasing carrier velocity and the particle velocity variance increases. The variance increase mechanism is similar to the first stage and the uniform flow, in which a time varying carrier velocity in combination with a random forcing leads to a variance increase in the particle velocity. In the stagnating flow, the random particle cloud compresses with a decreasing position variance before the wall is reached.

As opposed to the uniform flow case the carrier flow's velocity fluctuation, u', for the stagnation flow is non-zero which affects several terms in the moment equations. Even with these extra terms, just like for the uniform flow, the mean stagnation flow solution described by (8) and (9) can also be approximated by the solution of the deterministic equation for $a = \bar{a}$. The latter position and velocity solution have a root mean square deviation of 0.0073 for $\bar{x}_p$ and 0.0053 for $\bar{u}_p$ as compared to the former. Both the terms $\overline{\phi' u'}$ and $\overline{\phi' u'_p}$ turn out to be negligible in (9).

The evolution of the velocity variance as governed by its moment equation (11) is affected by the second term on the right hand side,

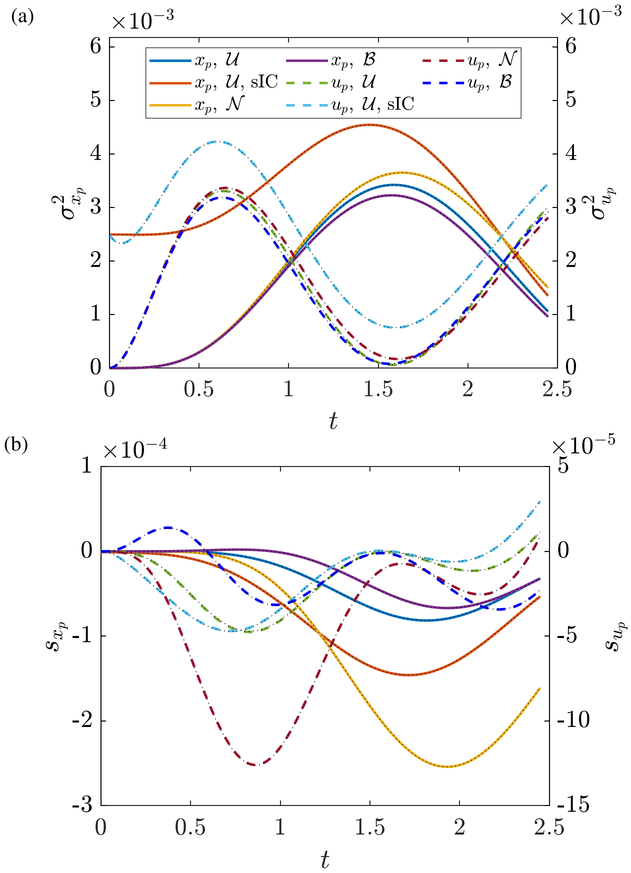

FIG. 15. Computations for the SFR case with MC in color lines and with the MoM in black dots of the (a) second and (b) third central moments for the particle position and velocity and the three distributions considered for a (see Fig. 6) and dIC. It is included the case of sIC for the uniform distribution. The legend in (a) is valid for (b) as well.

i.e., $\overline{\phi' u_p'}(\bar{u} - \bar{u}_p)$. At $t \sim 1.6$, the relative velocity $(\bar{u} - \bar{u}_p)$ in this term changes sign when the particle phase begins to decelerate after its initial acceleration. The sign of $\overline{\phi' u_p'}$ in this term changes at $t \sim 1.6$ also as follows: in the first stage u_p is monotonically increasing for all the forcing values of $\phi = a$ according to the analytical velocity solution (32); in stage two, some particles are accelerating and others are decelerating which yields different signs for $du_p/d\phi$ depending on ϕ. Upon ensemble averaging, it turns out that the mean of $du_p/d\phi$ is positive prior to $t \sim 1.6$ and negative after. In the third stage, u_p is monotonically decreasing with respect to ϕ. So, the correlation term $\overline{\phi' u_p'}$ changes sign at $t \sim 1.6$ and thus the term $\overline{\phi' u_p'}(\bar{u} - \bar{u}_p) > 0$.

In addition to the damping term that was discussed for the uniform flow case, the first term on the right hand side in the velocity variance equations (11) also involves the term $\bar{\phi}\overline{u' u_p'}$ for the stagnation flow case. Similar to the sign change of $\overline{\phi' u_p'}$ at $t \sim 1.6$, the sign of $\bar{\phi}\overline{u' u_p'}$ is the same as $\bar{u} - \overline{u_p}$ because of a comparable behavior of du_p/du and $du_p/d\phi$. As a result, $\bar{\phi}\overline{u' u_p'}$ is negative before $t \sim 1.6$ and positive thereafter. The values of the term $\overline{u' u_p'}$ are between –0.002 and 0.002 and are thus of the same order as the velocity variance $\sigma^2_{u_p}$ [see Fig. 15(a)]. The term $\bar{\phi}\overline{u' u_p'}$ therefor has a significant effect on the variance dynamics. At early times, it reduces the growth of the variance, and at later times it enhances growth as compared to the uniform flow where the term is zero.

The third order correlation terms (the third and fourth term in (11)) are observed to have a negligible contribution to the particle variance evolution. In comparing the maximum magnitude of each of the terms in the right hand side of (11) with respect to the left hand side over the time interval, we find that the terms $\overline{\phi' u' u_p'}$ and $\overline{u' u_p'^2}$ have at most a 3.0% and 1.0% contribution, whereas the first and second terms have a significant 120% and 152% contribution to the "variance acceleration."

Figures 15(a) and 15(b) include the variance evolution for several distribution functions of the forcing f_a. As in the uniform flow case, the effect of the shape of f_a is small on the order of 5% in the velocity variance and slightly more (order of 10%) in the position variance. The general trends are not affected by the shape of the forcing PDF.

The third position moment is negative throughout the time interval considered [Fig. 15(b)], indicating a non-symmetric position distribution that is skewed toward larger values of the particle coordinate. To understand the evolution of the particle velocity's third moment, we differentiate between two stages; first, when the mean interphase velocity $\bar{u} - \bar{u}_p$ is positive and the skewness shows a bias toward higher velocity values similar to the uniform flow case as also illustrated in Fig. 1. Second, when $\bar{u} - \bar{u}_p \sim 0$ at first after which it becomes negative, i.e., $\bar{u} - \bar{u}_p < 0$ with a near zero skewness first and decreasing after showing a bias toward small values of the particle coordinate when $\bar{u} - \bar{u}_p < 0$ right before the particles hit the wall. This second stage can be also understood through the evolution of the PDF that consists of the formation of the singular Dirac delta distribution for which the skewness is zero and its consequent behavior as illustrated in Fig. 1(b) with a change of the bias in the PDF.

Like in the uniform flow case, the evolution of the third central moment is affected by many different terms in the velocity skewness equation (13) as shown in Fig. 16. The fourth order correlation terms are important in the stagnation flow also, but because the velocity fluctuation is non-zero, $u' \neq 0$, the evolution of terms that involve u' are non-trivial and require a separate and more in-depth analysis. We feel this is outside the scope of the current paper and we plan to report on the skewness behavior in more detail in future work.

Stochastic initial conditions do not only alter the evolution of the mean of the stagnation flow solution with dIC by a constant offset as was the case for the uniform flow (see Fig. 14), but the difference between the solutions with dIC and sIC changes considerably over the time interval and specifically at early times. The variance of the particle position and velocity is initially offset according to its initial values as shown in Fig. 15(a), but then the difference with respect to the dIC case decreases as time evolves. This reduction can be understood by considering the stagnation flow solution where particles can nonphysically cross the wall (i.e., an opposed jet flow). For this flow, all particles move toward the same final state with $x_p = 0$ and $u_p = 0$ in the asymptotic time limit, $t \to \infty$, and thus the position and velocity variance tend to zero.

Between the initial time and the infinite time, the terms $\overline{x_p' u_p'}$ and $\overline{u' u_p'}$ are responsible for the reduced variances. The contribution of $\overline{u' u_p'}$ which is negative for $t < 1.6$, particularly, causes a greater increase in the damping term for sIC as compared to dIC at early times. When

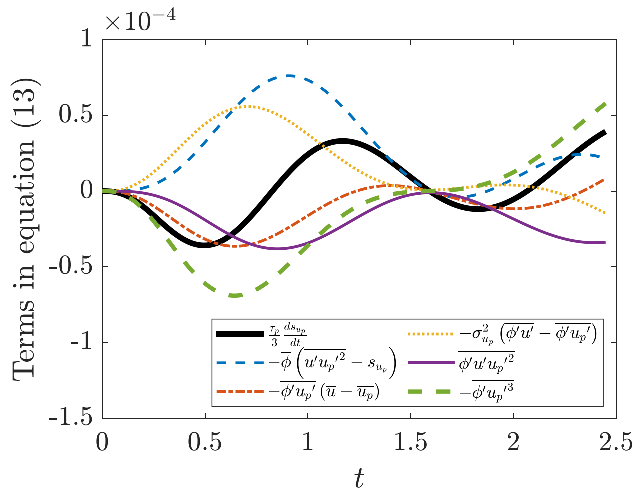

FIG. 16. Terms in Eq. (13) vs time t for the SFR case with dIC and a uniform forcing distribution.

the interphase velocity changes sign at $t \sim 1.6$, this term becomes positive and it will have the opposite effect. A physical interpretation is as follows: a more energetic initial state with higher velocity variance is more resistant to changes induced by stochastic forcing resulting in greater damping at early times. The term $\overline{x_p' u_p'}$ is positive in the acceleration stage and negative in the deceleration stage and its magnitude is greater for dIC as compared to sIC consistent with greater values of u_p' for sIC.

Another considerable difference between the dIC and sIC is that the minimum in the velocity variance at $t \sim 1.6$ is non-zero for the stochastic case, while it is nearly zero for the deterministic case. As a consequence, the singularity in the distribution function when the relative velocity changes sign can be expected to be less significant and the PDF can be expected to have a broader support.

2. SFR case: Method of distributions

Using the same grid as was used for the uniform flow case, the PDF solution for the SFR case with a uniform forcing distribution, f_a, and dIC are computed and plotted for three instances in Fig. 17 at $t = 1.22$, $t = 1.60$, and $t = 2.15$. At time $t = 0$, the initial condition is identical to the uniform flow case plotted in Fig. 11(a), and it is therefore not repeated in Fig. 17. The MC results are also plotted in Fig. 17, and they are in excellent agreement with the MoD results.

During the first stage ($t < 0.6$), the joint PDF $f_{x_p u_p}$ deforms along the mean of the particle trajectory (depicted by the black solid line), showing a non-linear clustering of the particles in the $X_p - U_p$ plane toward high values. During the second stage ($0.6 < t < 1.6$), some particles accelerate and others decelerate leading to the near singular Dirac delta distribution at $t \sim 1.6$ [Fig. 17(b)]. At later times ($t > 1.6$), the PDF of the particle velocity increases on the left front [Fig. 17(c)], confirming a bias toward lower velocities in a deceleration field as discussed in the MC results.

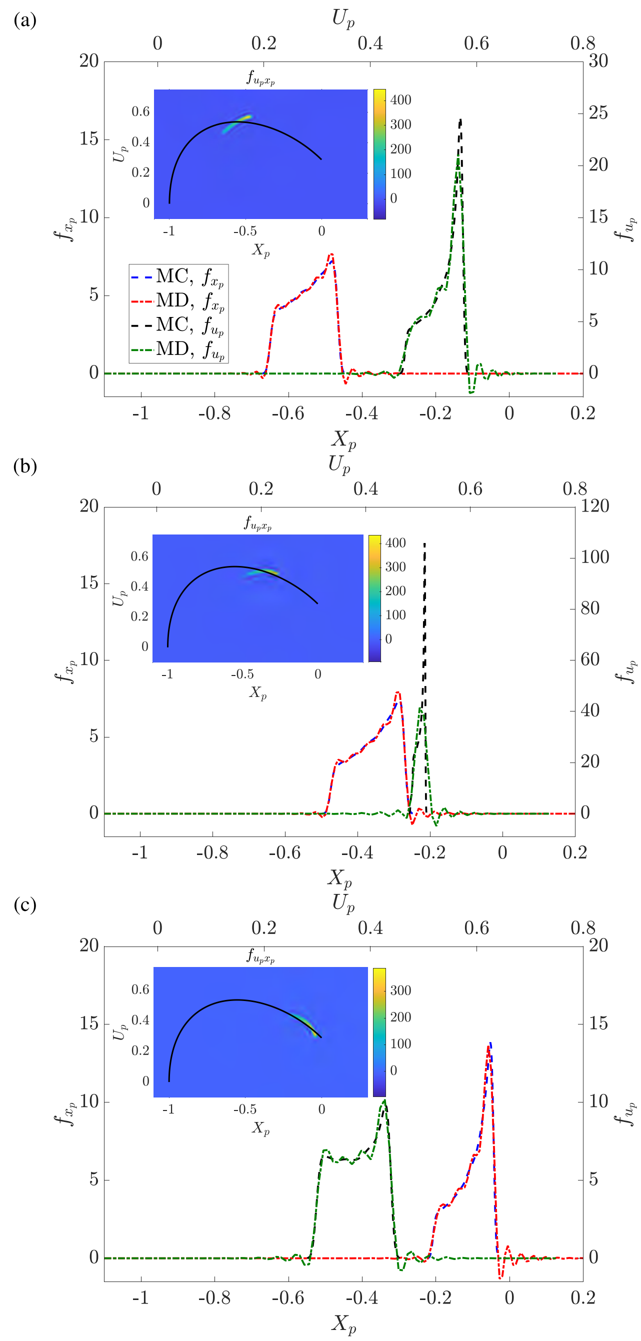

FIG. 17. Marginals f_{x_p} and f_{u_p} at $t = [1.22, 1.60, 2.15]$ in (a), (b), and (c), respectively, for the SFR test case with dIC and the uniform distribution for f_a. Contour plots are of the joint PDF $f_{x_p u_p}$ superposed with the mean of the particle phase solution.

The position PDF solution has an increasing bias toward the large value of X_p which is consistent with the asymptotic infinite time behavior of the nonphysical solution where particles are permitted to cross the wall and where both the particle velocity and position distribution evolve to a Dirac delta centered at $X_p = 0$ and $U_p = 0$.

3. SFF case: Monte Carlo results

In a final test, the particle velocity is initialized with the carrier phase velocity at the particle position. The MC results for the mean with a two standard deviation bandwidth are plotted vs time in Fig. 18. In the SFF case, the particle phase only decelerates which yields an evolution that is opposite to the uniform flow evolution as plotted in Fig. 1(a) or an evolution that is very similar to the third "deceleration" stage of the SFR case for $t > 1.6$. The mean velocity decreases monotonically when the mean particle position increases toward the wall. This evolution is accompanied by an increase in the variances of both x_p and u_p.

Because the SFF case is similar to the other two cases, the moment evolution results do not shed any additional light on the evolution of the stochastically forced particle phase. It is therefore omitted here. For completeness, we include the plots for evolution of the moments in Appendix C (Figs. 20 and 21).

4. SFF case: Method of distributions

The results for the uniform distribution forcing, f_a, for the SFF case are also very similar to the deceleration stage of the SFR case. Rather than reiterating that discussion, we choose a different stochastic forcing according to a beta distribution for f_a in Fig. 6 which does not have steep gradients in f_a like the uniform distribution. For a grid with the same size as described before, the distribution results for two different times are shown in Figs. 19(a) and 19(b) with a deterministic initial condition. Clearly, the solution does not show Gibbs oscillations and the MC results and the MoD are in excellent agreement.

As time evolves, the PDF of the particle position is advected with a positive characteristic velocity (14) and the particle velocity with a negative velocity according to (15). The PDFs widen in time as the response times of random particles is different for different stochastic forcing leading to variations in the particles velocities and positions. Both the position and velocity PDF display a non-Gaussian (non-symmetric) trend that is more subtle than for the uniform forcing.

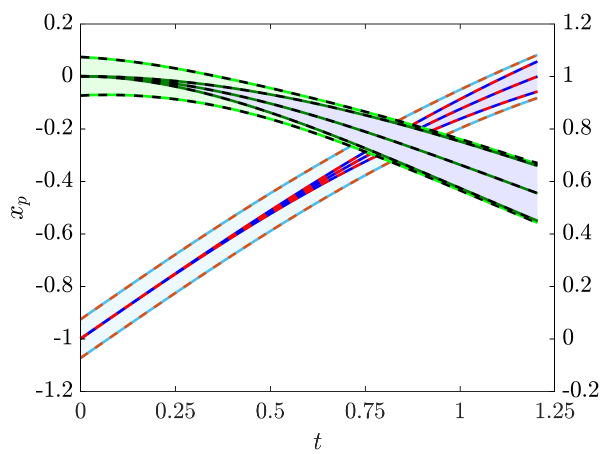

FIG. 18. Two standard deviation interval along the mean for the test case SFF with a uniform forcing distribution. In dashed green, the particle velocity computed with the MoD and in black with MC. In dashed red, the particle position computed with MoD and in blue with MC. Dark colors indicate dIC, whereas light ones indicate sIC.

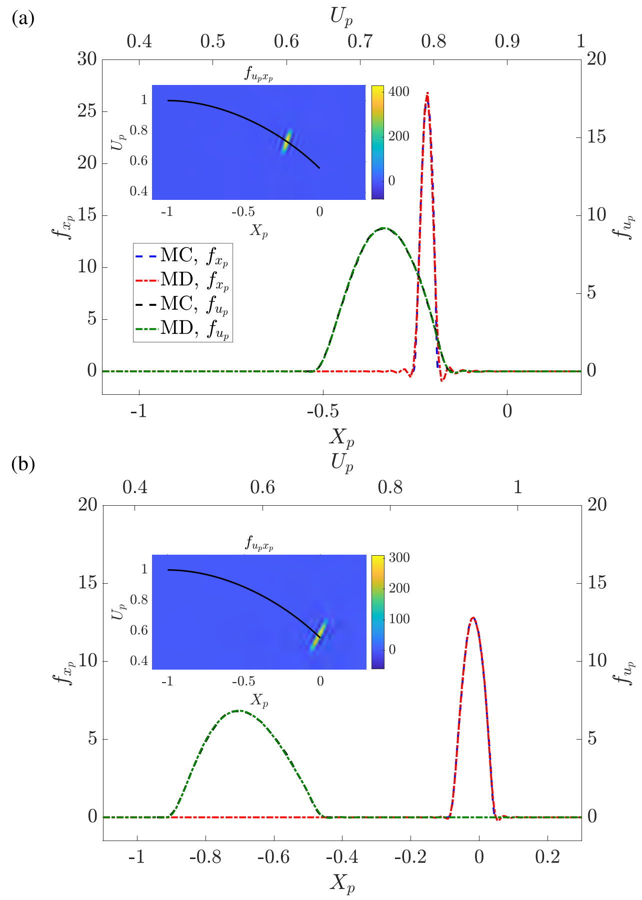

FIG. 19. Marginals f_{x_p} and f_{u_p} at $t = [0.87, 1.17]$ in (*a*) and (*b*), respectively, for the SFR test case with dIC and a uniform forcing distribution. Contours of the joint PDF $f_{x_p u_p}$ superposed with the mean of the particle phase solution.

VII. CONCLUDING REMARKS

Several techniques and models including a Monte Carlo approach, a method of moments, and a method of distributions are developed and compared for analysis of particle dynamics with stochastic forcing in one-way coupled Eulerian–Lagrangian formulations. Random solutions of two canonical flow problems are discussed including a particle phase accelerated in a uniform carrier flow and a particle phase released in a stagnation carrier flow with two initial conditions, one at rest and one initialized at the carrier flow velocity.

Starting from the Lagrangian particle equations for position and velocity with stochastic forcing, a closed PDF formulation is derived. A single hyperbolic partial differential equation, whose characteristic advection velocities are non-constant, governs the evolution of the PDF solution. In a single spatial dimension, the PDF depends on three variables at a given time, including the position, the velocity, and a forcing coefficient.

A high-order spectral method with discontinuity regularization is necessary for the accurate solution of the hyperbolic partial differential equation that admits discontinuities. A polynomial regularization of a Dirac delta function with m vanishing moments is shown to accurately capture the first m moments of the PDF solution in time.

Moment equations are derived for the first three moments of the particle position and velocity, representing the mean, variance, and skewness of the PDF. Monte Carlo results are used to determine correlations terms and to close the system of moment equations.

Analytical solutions are derived for the system of two linear ODEs that govern the dynamics of particles with a deterministic forcing in a one-dimensional uniform flow and stagnation flow. The particle solution in the stagnation flow has its final state with a zero velocity at the wall. Depending on the relative forcing, the particle manifolds in the phase space (position/velocity space) tend to either a node or spiral.

The mean solution with random forcing can be approximated within 1% using a mere single deterministic solution at the mean forcing for all flow cases considered.

In flows where all randomly forced particles accelerate or decelerate, the velocity variance increases driven by a single correlation source term. A damping terms counters this source term. When the particle velocity settles, the velocity variance reduces to zero because of this damping. Higher-order correlation terms are generally negligible in the velocity variance equation. The position variance increases in accelerating flows and decreases in decelerating flows, i.e., the random cloud expands and compresses, respectively. When the relative velocity changes sign, the particle variance approaches zero and the PDF has a very narrow support.

The skewness of the distribution function has a bias toward the carrier velocity to which the particle accelerates or decelerates. The bias of the distribution function is non-linear and more significant toward to the tail ends of the distribution function. The skewness equation is driven by a sourcing and a damping similar to the variance equation, but with different response times. High-order correlation terms are significant, suggesting a complicated tail behavior of the PDF.

In near future work, we intend to report on the tail behavior of the PDF solution of the particle phase. We also plan to develop distribution function models for two-way couple Eulerian–Lagrangian formulations.

ACKNOWLEDGMENTS

This work was supported in part by the Air Force Office of Scientific Research under Award Nos. FA9550-19-1-0387 and FA9550-18-1-0474.

APPENDIX A: DERIVATION OF THE PDF EQUATION USING THE METHOD OF DISTRIBUTIONS

Here, a PDF equation is developed to solve the stochastic system defined by (1) with the so-called method of distributions. First, we define the fine-grained JPDF Π as

$$\Pi(A,a;X_p,x_p;U_p,u_p;t)=\delta(A-a)\delta(X_p-x_p(t))\delta\big(U_p-u_p(t)\big), \tag{A1}$$

where A, X_p, and U_p are deterministic magnitudes and $\delta(\cdot)$ is the Dirac delta function. Taking the derivative of Π with respect to time and using the chain rule and the Dirac delta properties, we find

$$\frac{\partial\Pi}{\partial t}=\frac{dx_p}{dt}\frac{\partial\Pi}{\partial x_p}+\frac{du_p}{dt}\frac{\partial\Pi}{\partial u_p}=-\frac{dx_p}{dt}\frac{\partial\Pi}{\partial X_p}-\frac{du_p}{dt}\frac{\partial\Pi}{\partial U_p}, \tag{A2}$$

where we can make use of (1) for writing

$$\frac{\partial\Pi}{\partial t}+u_p\frac{\partial\Pi}{\partial X_p}+\frac{ag(u-u_p)}{\tau_p}(u-u_p)\frac{\partial\Pi}{\partial U_p}=0, \tag{A3}$$

that in conservative form is

$$\frac{\partial\Pi}{\partial t}+\frac{\partial}{\partial X_p}(u_p\Pi)+\frac{\partial}{\partial U_p}\left[\frac{ag(u-u_p)}{\tau_p}(u-u_p)\Pi\right]=0. \tag{A4}$$

Defining the ensemble mean of an integrable function $h(a,x_p,u_p)$ with the joint PDF $f_{ax_pu_p}$ as

$$E\big[h(a,x_p,u_p)\big]=\iiint_{-\infty}^{\infty}h(A',X_p',U_p)f_{ax_pu_p}(A',X_p',U_p';t)\mathrm{d}A'\mathrm{d}X_p'\mathrm{d}U_p', \tag{A5}$$

the ensemble of the function Π for a particular set of the deterministic variables is obtained as

$$\begin{aligned}E[\Pi]&=\iiint_{-\infty}^{\infty}\Pi(A,A';X_p,X_p',U_p,U_p';t)\\&\quad\times f_{ax_pu_p}(A',X_p',U_p';t)dA'dX_p'dU_p'\\&=\iiint_{-\infty}^{\infty}\delta(A-A')\delta(X_p-X_p')\delta(U_p-U_p')\\&\quad\times f_{ax_pu_p}(A',X_p',U_p';t)dA'dX_p'dU_p'\\&=f_{ax_pu_p}(A,X_p,U_p;t).\end{aligned} \tag{A6}$$

This procedure suggests how to obtain a partial differential equation for $f_{ax_pu_p}$ from (A4) taking the ensemble mean each term. To do so, we need to use the property that allows us to exchange expectation with derivatives respect to deterministic variables. For example, for the deterministic variable time, one has

$$E\left[\frac{\partial h(a,x_p,u_p)}{\partial t}\right]=\frac{\partial E\big[h(a,x_p,u_p)\big]}{\partial t}. \tag{A7}$$

Using this property, the ensemble mean of the first term in (A4) is trivial

$$E\left[\frac{\partial\Pi}{\partial t}\right]=\frac{\partial f_{ax_pu_p}}{\partial t}. \tag{A8}$$

The second is calculated as

$$E\left[\frac{\partial(u_p\Pi)}{\partial X_p}\right] = \frac{\partial}{\partial X_p}E[u_p\Pi] \tag{A9}$$

$$= \frac{\partial}{\partial X_p}\left[\iiint_{-\infty}^{\infty} U_p'\Pi(A,A';X_p,X_p';U_p,U_p';t) \times f_{ax_pu_p}(A',X_p',U_p';t)dA'dX_p'dU_p'\right] \tag{A10}$$

$$= \frac{\partial}{\partial X_p}\left[\iiint_{-\infty}^{\infty} U_p'\delta(A-A')\delta(X_p-X_p')\delta(U_p-U_p') \times f_{ax_pu_p}(A',X_p',U_p';t)dA'dX_p'dU_p\right] \tag{A11}$$

$$= \frac{\partial}{\partial X_p}\left(U_p f_{ax_pu_p}\right). \tag{A12}$$

In the same way, the third term is

$$E\left[\frac{\partial}{\partial U_p}\left(\frac{ag(u-u_p)}{\tau_p}(u-u_p)\Pi\right)\right] = \frac{\partial}{\partial U_p}\left(\frac{Ag(U-U_p)}{\tau_p}(U-U_p)f_{ax_pu_p}\right), \tag{A13}$$

where for coherence we make use of U as the deterministic value of the carrier flow. In this study, the carrier flow is considered deterministic and therefore $u = U$.

Finally, the deterministic equation that governs the joint probability density function of the solution is

$$\frac{\partial f_{ax_pu_p}}{\partial t} + \frac{\partial}{\partial X_p}\left(U_p f_{ax_pu_p}\right) + \frac{\partial}{\partial U_p}\left(\frac{Ag(U-U_p)}{\tau_p}(U-U_p)f_{ax_pu_p}\right) = 0. \tag{A14}$$

This equation has to be solved with deterministic or stochastic initial conditions defined by (7) or (6) and also be marginalized according to

$$f_{x_pu_p}(X_p,U_p;t) = \int_{-\infty}^{\infty} f_{ax_pu_p}(A,X_p,U_p;t)dA, \tag{A15}$$

$$f_{x_p}(X_p;t) = \int_{-\infty}^{\infty} f_{x_pu_p}(X_p,U_p;t)dU_p, \tag{A16}$$

$$f_{u_p}(U_p;t) = \int_{-\infty}^{\infty} f_{x_pu_p}(X_p,U_p;t)dX_p. \tag{A17}$$

We also define here the n^{th} moment about c of a continuum random variable x with PDF $f_x(x)$ as

$$\mu_n = \int_{-\infty}^{\infty}(x-c)^n f_x(x)dx, \tag{A18}$$

where if $n = 1$ and $c = 0$, we obtain the mean μ_x, and if c is selected to be the mean, we find the n^{th} central moment of f_x.

APPENDIX B: DETERMINISTIC ANALYTICAL SOLUTION OF THE TEST CASES

1. Uniform flow

For the uniform flow where u is constant, the system of Eq. (1) can be expressed as a first order ODE system with constant coefficients for $x_p(t)$ and $u_p(t)$

$$\frac{d}{dt}\begin{bmatrix} x_p \\ u_p \end{bmatrix} = \begin{bmatrix} 0 & 1 \\ 0 & -b \end{bmatrix}\begin{bmatrix} x_p \\ u_p \end{bmatrix} + \begin{bmatrix} 0 \\ bu \end{bmatrix}, \tag{B1}$$

a second order ODE for $x_p(t)$

$$\frac{d^2x_p}{dt^2} + b\frac{dx_p}{dt} = bu, \tag{B2}$$

a first order ODE for $u_p(t)$

$$\frac{du_p}{dt} + bu_p = bu, \tag{B3}$$

or as a differential equation of separable variables for the phase space $u_p(x_p)$ as the system (1) becomes autonomous

$$\frac{du_p}{dx_p} = \frac{b(u-u_p)}{u_p}. \tag{B4}$$

The analytical solution of $x_p(t)$ and $u_p(t)$ is trivially obtained solving any of the above options as

$$x_p(t) = x_{p_0} + ut + \frac{1}{b}(u-u_{p_0})(e^{-bt}-1), \tag{B5}$$

$$u_p(t) = u + (u_{p_0}-u)e^{-bt}. \tag{B6}$$

The time can be removed combining the last two equations to find the solution in the particle phase as $u_p(x_p)$.

2. Stagnation flow

For the centerline of the stagnation flow $y = 0$, the carrier flow is $u = -kx = -kx_p$ after interpolating at the particle location according to Hiemenz solution.[50] The system (1) can be described as a first ODE system of constant coefficients

$$\frac{d}{dt}\begin{bmatrix} x_p \\ u_p \end{bmatrix} = \begin{bmatrix} 0 & 1 \\ -kb & -b \end{bmatrix}\begin{bmatrix} x_p \\ u_p \end{bmatrix}, \tag{B7}$$

a second order ODE for $x_p(t)$

$$\frac{d^2x_p}{dt^2} + b\frac{dx_p}{dt} + kbx_p = 0, \tag{B8}$$

or an integrable equation for the particle phase $u_p(x_p)$

$$\frac{du_p}{dx_p} = -\frac{b(kx_p+u_p)}{u_p}. \tag{B9}$$

Writing the system (B7) as $\mathbf{z}'(t) = B\mathbf{z}(\mathbf{t})$, with the initial condition $\mathbf{z}(0) = \mathbf{z}_0$, where

$$\mathbf{z}'(t) = \begin{bmatrix} x_p(t) \\ u_p(t) \end{bmatrix}, \quad \mathbf{z}_0 = \begin{bmatrix} x_{p_0} \\ u_{p_0} \end{bmatrix}, \quad B = \begin{bmatrix} 0 & 1 \\ -bk & -b \end{bmatrix}, \tag{B10}$$

the analytical solution is given by

$$\mathbf{z}(t) = e^{Bt}\mathbf{z}_0. \tag{B11}$$

Using the eigen decomposition $B = S\Lambda S^{-1}$, the exponential matrix can be obtained as

$$e^{Bt} = Se^{\Lambda t}S^{-1}, \tag{B12}$$

with

$$S = \begin{bmatrix} \dfrac{-1+\sqrt{b-4k}}{2k\sqrt{b}} & \dfrac{-1-\sqrt{b-4k}}{2k\sqrt{b}} \\ 1 & 1 \end{bmatrix}, \quad \Lambda = \begin{bmatrix} \lambda_1 & 0 \\ 0 & \lambda_2 \end{bmatrix}, \tag{B13}$$

and

$$\lambda_1 = \frac{-b-\sqrt{b(b-4k)}}{2}, \quad \lambda_2 = \frac{-b+\sqrt{b(b-4k)}}{2}. \tag{B14}$$

Finally, the exponential matrix is

$$e^{\Lambda t} = \begin{bmatrix} e^{\lambda_1 t} & 0 \\ 0 & e^{\lambda_2 t} \end{bmatrix}, \tag{B15}$$

and the analytical solution can be expressed as

$$x_p(t) \quad = e^{-\dfrac{bt}{2}}\left[\frac{bx_{p_0}+2u_{p_0}}{\gamma}\sinh\left(\frac{t\gamma}{2}\right) + x_{p_0}\cosh\left(\frac{t\gamma}{2}\right)\right], \tag{B16}$$

and

$$u_p(t) = \frac{1}{2\gamma}e^{-\frac{t(\gamma+b)}{2}}\left[u_{p_0}\gamma(e^{\gamma t}+1) - b(e^{\gamma t}-1)(2kx_{p_0}+u_{p_0})\right], \tag{B17}$$

where $\gamma = \sqrt{b}\sqrt{b-4k}$.

Just for completion, in the case $b = 4k$, the matrix S is singular, and the Jordan decomposition $B = MJM^{-1}$ is required[52] to find the exponential matrix defined as $e^{Bt} = Me^{Jt}M^{-1}$ with

$$M = \begin{bmatrix} -1/(2k) & -1/(4k^2) \\ 1 & 0 \end{bmatrix}, \quad J = \begin{bmatrix} -2k & 1 \\ 0 & -2k \end{bmatrix}, \tag{B18}$$

so that one has

$$e^{Jt} = \begin{bmatrix} e^{-2kt} & e^{-2kt}t \\ 0 & e^{-2kt} \end{bmatrix}, \tag{B19}$$

and the analytical solution changes to

$$x_p(t) = e^{-2kt}\left[x_{p_0} + t\left(2kx_{p_0}+u_{p_0}\right)\right], \tag{B20}$$

$$u_p(t) = e^{-2kt}\left[u_{p_0} - 2kt\left(2kx_{p_0}+u_{p_0}\right)\right]. \tag{B21}$$

APPENDIX C: MOMENT RESULTS FOR THE SFF CASE

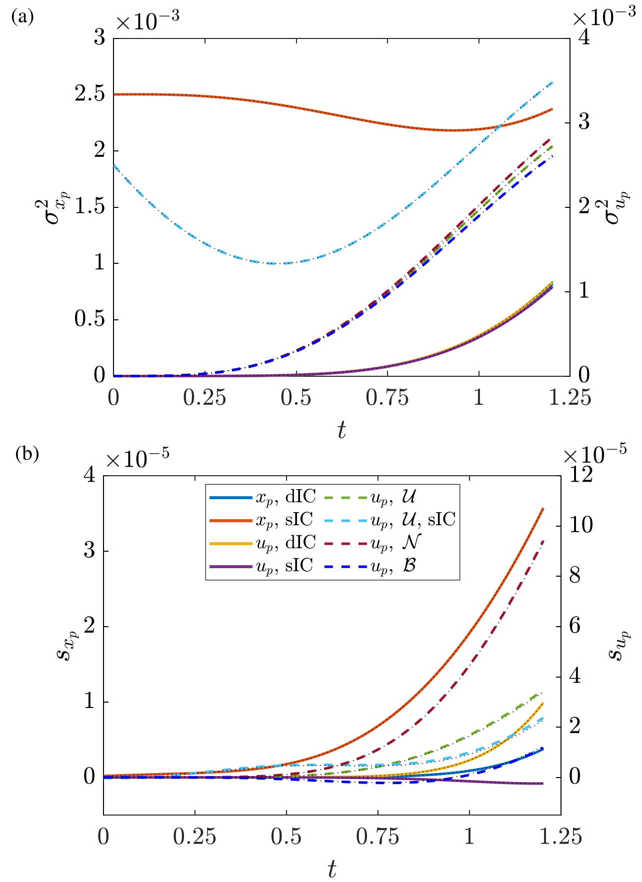

FIG. 20. Computations for the SFF case with MC in color lines and with the MoM in black dots of the (a) second and (b) third central moments for the particle position and velocity and the three distributions considered for *a* (see Fig. 6) and dIC. The case of sIC for the uniform distribution is included. The legend in (b) is valid for (a) as well.

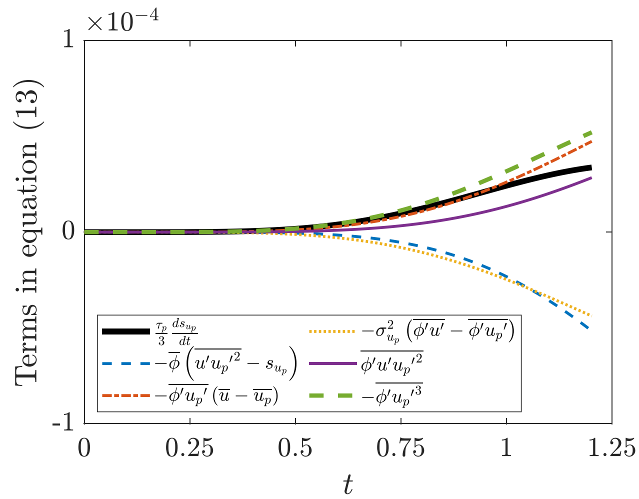

FIG. 21. Terms in (13) vs time *t* for the SFF with dIC.

DATA AVAILABILITY

The data that support the findings of this study are available from the corresponding author upon reasonable request.

REFERENCES

[1]C. T. Crowe, M. P. Sharma, and D. E. Stock, "The particle-source-in cell (PSI-CELL) model for gas-droplet flows," J. Fluids Eng. **99**(2), 325–332 (1977).
[2]O. Sen, S. Davis, G. B. Jacobs, and H. S. Udaykumar, "Evaluation of convergence behavior of metamodeling techniques for bridging scales in multi-scale multimaterial simulation," J. Comput. Phys. **294**, 585–604 (2015).
[3]O. Sen, N. J. Gaul, K. K. Choi, G. B. Jacobs, and H. S. Udaykumar, "Evaluation of kriging surrogate models constructed from mesoscale computations of shock interactions with particles," J. Comput. Phys. **336**, 235–260 (2017).
[4]S. Davis, O. Sen, G. B. Jacobs, and, and H. S. Udaykumar, "Coupling of micro-scale and macro-scale Eulerian-Lagrangian models for the computation of shocked particle-laden flows," In *ASME International Mechanical Engineering Congress and Exposition* (American Society of Mechanical Engineers, 2013), Vol. 56314, p. V07AT08A011.
[5]S. Lomholt and M. R. Maxey, "Force-coupling method for particulate two-phase flow: Stokes flow," J. Comput. Phys. **184**, 381–405 (2003).
[6]G. S. Shallcross, R. O. Fox, and J. Capecelatro, "A volume-filtered description of compressible particle-laden flows," Int. J. Multiphase Flow **122**, 103138 (2020).
[7]C. T. Crowe, M. Sommerfeld, and Y. Tsuji, *Multiphase Flows with Droplets and Particles* (CRC Press LLC, Boca Raton, FL, 1998).
[8]J. D. Anderson, *Modern Compressible Flow: with Historical Perspective*, Number Book (McGraw-Hill, 1990).
[9]G. G. Stokes, *On the Effect of the Internal Friction of Fluids on the Motion of Pendulums* (Pitt Press Cambridge, 1851), Vol. 9.
[10]M. R. Maxey and J. J. Riley, "Equation of motion for a small rigid sphere in a nonuniform flow," Phys. Fluids **26**, 883–889 (1983).
[11]V. M. Boiko and S. V. Poplavskii, "Drag of nonspherical particles in a flow behind a shock wave," Combust. Explos. Shock Waves **41**(1), 71–77 (2005).
[12]E. Loth, "Compressibility and rarefaction effects on drag of a spherical particle," AIAA J. **46**(9), 2219–2228 (2008).
[13]G. Tedeschi, H. Gouin, and M. Elena, "Motion of tracer particles in supersonic flows," Exp. Fluids **26**(4), 288–296 (1999).
[14]Z. G. Feng, E. E. Michaelides, and S. Mao, "On the drag force of a viscous sphere with interfacial slip at small but finite Reynolds numbers," Fluid Dyn. Res. **44**(2), 025502 (2012).
[15]W. E. Ranz and W. R. Marshall, Jr., "Evaporation from drops, Part II," Chem. Eng. Prog. **48**, 173–180 (1952).
[16]O. Sen, N. J. Gaul, K. K. Choi, G. B. Jacobs, and H. S. Udaykumar, "Evaluation of multifidelity surrogate modeling techniques to construct closure laws for drag in shock–particle interactions," J. Comput. Phys. **371**, 434–451 (2018).
[17]G. B. Jacobs and H. S. Udaykumar, "Uncertainty quantification in Eulerian-Lagrangian simulations of (point-) particle-laden flows with data-driven and empirical forcing models," Int. J. Multiphase Flow **121**, 103114 (2019).
[18]W. C. Moore, S. Balachandar, and G. Akiki, "A hybrid point–particle force model that combines physical and data–driven approaches," J. Comput. Phys. **385**, 187–208 (2019).
[19]A. Seyed-Ahmadi and A. Wachs, "Microstructure–informed probability–driven point–particle model for hydrodynamic forces and torques in particle–laden flows," J. Fluid Mech. **900**, A21 (2020).
[20]S. Taverniers and D. M. Tartakovsky, "Estimation of distributions via multi-level Monte Carlo with stratified sampling," J. Comput. Phys. **419**, 109572 (2020).
[21]S. Taverniers, S. B. M. Bosma, and D. M. Tartakovsky, "Accelerated multilevel Monte Carlo with kernel-based smoothing and Latinized stratification," Water Resour. Res. **56**(9), e2019WR026984, https://doi.org/10.1029/2019WR026984 (2020).
[22]X. Ma and N. Zabaras, "An adaptive hierarchical sparse grid collocation algorithm for the solution of stochastic differential equations," J. Comput. Phys. **228**(8), 3084–3113 (2009).
[23]D. A. Barajas-Solano and D. M. Tartakovsky, "Stochastic collocation methods for nonlinear parabolic equations with random coefficients," SIAM/ASA J. Uncertainty Quantif. **4**(1), 475–494 (2016).
[24]X. Wan and G. E. Karniadakis, "An adaptive multi-element generalized polynomial chaos method for stochastic differential equations," J. Comput. Phys. **209**(2), 617–642 (2005).
[25]X. Wan and G. E. Karniadakis, "Multi-element generalized polynomial chaos for arbitrary probability measures," SIAM J. Sci. Comput. **28**(3), 901–928 (2006).
[26]D. Venturi, X. Wan, and G. E. Karniadakis, "Stochastic bifurcation analysis of Rayleigh-Bénard convection," J. fluid mechanics **650**, 391–413 (2010).
[27]B. Debusschere, *Intrusive Polynomial Chaos Methods for Forward Uncertainty Propagation* (Springer International Publishing, Cham, 2017), pp. 617–636.
[28]M. Ye, S. P. Neuman, A. Guadagnini, and D. M. Tartakovsky, "Nonlocal and localized analyses of conditional mean transient flow in bounded, randomly heterogeneous porous media," Water Resour. Res. **40**, W05104, https://doi.org//10.1029/2003WR002099 (2004).
[29]T. Maltba, P. Gremaud, and D. M. Tartakovsky, "Nonlocal PDF methods for langevin equations with colored noise," J. Comput. Phys. **367**, 87–101 (2018).
[30]T. S. Lundgren, "Distribution functions in the statistical theory of turbulence," Phys. Fluids **10**(5), 969–975 (1967).
[31]D. M. Tartakovsky and P. A. Gremaud, "Method of distributions for uncertainty quantification," in *Handbook of Uncertainty Quantification*, edited by R. Ghanem, D. Higdon, and H. Owhadi (Springer, New York, 2015), pp. 763–783.
[32]R. J. Rutjens, G. B. Jacobs, and D. M. Tartakovsky, "Method of distributions for systems with stochastic forcing," arXiv:1909.01774 (2019).
[33]P. Wang and D. M. Tartakovsky, "Uncertainty quantification in kinematic-wave models," J. Comput. Phys. **231**(23), 7868–7880 (2012).
[34]P. Wang, D. M. Tartakovsky, Jr. K. D. Jarman, and A. M. Tartakovsky, "CDF solutions of Buckley-Leverett equation with uncertain parameters," Multiscale Model. Simul **11**(1), 118–133 (2013).
[35]A. Alawadhi, F. Boso, and D. M. Tartakovsky, "Method of distributions for water-hammer equations with uncertain parameters," Water Resour. Res. **54**(11), 9398–9411, https://doi.org/10.1029/2018WR023383 (2018).
[36]F. Boso and D. M. Tartakovsky, "Data-informed method of distributions for hyperbolic conservation laws," SIAM J. Sci. Comput. **42**(1), A559–A583 (2020).
[37]H.-J. Yang, F. Boso, H. A. Tchelepi, and D. M. Tartakovsky, "Probabilistic forecast of single-phase flow in porous media with uncertain properties," Water Resour. Res. **55**(11), 8631–8645, https://doi.org/10.1029/2019WR026090 (2019).
[38]G. Haller, "Lagrangian coherent structures," Annu. Rev. Fluid Mech. **47**, 137–162 (2015).
[39]S. Jean-Piero and G. B. Jacobs, "Regularization of singularities in the weighted summation of Dirac-delta functions for the spectral solution of hyperbolic conservation laws," J. Sci. Comput. **72**(3), 1080–1092 (2017).
[40]B. W. Wissink, G. B. Jacobs, J. K. Ryan, W. S. Don, and E. T. A. van der Weide, "Shock regularization with smoothness-increasing accuracy-conserving Dirac-delta polynomial kernels," J. Sci. Comput. **77**(1), 579–596 (2018).
[41]G. B. Jacobs and W. S. Don, "A high-order WENO-Z finite difference based particle-source-in-cell method for computation of particle-laden flows with shocks," J. Comput. Phys. **228**(5), 1365–1379 (2009).
[42]S. L. Davis, G. B. Jacobs, O. Sen, and H. S. Udaykumar, "SPARSE-A subgrid particle averaged Reynolds stress equivalent model: Testing with a priori closure," Proc. R. Soc. A: Math., Phys. Eng. Sci. **473**(2199), 20160769 (2017).
[43]B. Shotorban, G. B. Jacobs, O. Ortiz, and Q. Truong, "An Eulerian model for particles nonisothermally carried by a compressible fluid," Int. J. Heat Mass Transfer **65**, 845–854 (2013).
[44]R. G. Patel, O. Desjardins, and R. O. Fox, "Three-dimensional conditional hyperbolic quadrature method of moments," J. Comput. Phys.: X **1**, 100006 (2019).
[45]S. Jean-Piero, G. B. Jacobs, and W. S. Don, "A high-order Dirac-delta regularization with optimal scaling in the spectral solution of one-dimensional singular hyperbolic conservation laws," SIAM J. Sci. Comput. **36**(4), A1831–A1849 (2014).

[46]K. Sengupta, B. Shotorban, G. B. Jacobs, and F. Mashayek, "Spectral-based simulations of particle-laden turbulent flows," Int. J. Multiphase Flow **35**(9), 811–826 (2009).
[47]D. Gottlieb and J. S. Hesthaven, "Spectral methods for hyperbolic problems," J. Comput. Appl. Math. **128**(1-2), 83–131 (2001).
[48]J. S. Hesthaven, S. Gottlieb, and D. Gottlieb, *Spectral Methods for Time-Dependent Problems* (Cambridge University Press, 2007), Vol. 21.
[49]S. Gottlieb and C. W. Shu, "Total variation diminishing Runge-Kutta schemes," Math. Comput. **67**(221), 73–85 (1998).
[50]K. Hiemenz, "Die Grenzschicht an einem in den gleichformigen Flussigkeitsstrom eingetauchten geraden Kreiszylinder," Dinglers Polytech. J. **326**, 321–324 (1911).
[51]L. Rosenhead, *Laminar Boundary Layers: An account of the Development, Structure, and Stability of Laminar Boundary Layers in Incompressible Fluids, Together with a Description of the Associated Experimental Techniques* (Dover Publications, 1988).
[52]B. Noble and J. W. Daniel, *Applied Linear Algebra* (Prentice-Hall Englewood Cliffs, NJ, 1977), Vol. 3.